The role of bed roughness in wave transformation across sloping rock shore platforms

Poate, Timothy G.; Masselink, G.; Austin, Martin; Dickson, Mark; McCall, Robert T.

Journal of Geophysical Research: Earth Surface

DOI:
10.1002/2017JF004277

Published: 01/01/2018

Peer reviewed version

1

THE ROLE OF BED ROUGHNESS IN WAVE TRANSFORMATION ACROSS SLOPING ROCK SHORE PLATFORMS

Tim Poate[1], *Gerd Masselink*[1], *Martin J. Austin*[2], *Mark Dickson*[3], *Robert McCall*[4]

[1] School of Biological and Marine Sciences, Plymouth University, Drake Circus, Plymouth, PL4 8AA, UK
[2] School of Ocean Sciences, Bangor University, Menai Bridge, Anglesey, LL59 5AB, UK
[3] School of Environment, The University of Auckland, Auckland 1142, New Zealand
[4] Department of Marine and Coastal Systems, Deltares, Boussinesqweg 1, 2629 HV Delft, the Netherlands

Corresponding author: Tim Poate (timothy.poate@plymouth.ac.uk)

Key Points:

- Extensive field dataset and numerical simulations exploring bed roughness on wave transformation
- Bed roughness not significant in the surf zone; therefore, friction can be neglected for short wave transformation on rocky platforms
- In model simulations, friction is only significant outside of the surf zone for very rough flat platforms and during small wave conditions.

Abstract

We present for the first time observations and model simulations of wave transformation across sloping (Type A) rock shore platforms. Pressure measurements of the water surface elevation using up to 15 sensors across five rock platforms with contrasting roughness, gradient and wave climate, represent the most extensive collected, both in terms of the range of environmental conditions, and the temporal and spatial resolution. Platforms are shown to dissipate both incident and infragravity wave energy as skewness and asymmetry develop and, in line with previous studies, surf zone wave heights are saturated and strongly tidally-modulated. Overall, the observed properties of the waves and formulations derived from sandy beaches does not highlight any systematic inter-platform variation, in spite of significant differences in platform roughness, suggesting that friction can be neglected when studying short wave transformation. Optimisation of a numerical wave transformation model shows that the wave breaker criterion falls between the range of values reported for flat sandy beaches and those of steep coral fore-reefs. However, the optimised drag coefficient shows significant scatter for the roughest sites and an alternative empirical drag model, based on the platform roughness, does not improve model performance. Thus, model results indicate that the parameterisation of frictional drag using the bottom roughness length-scale may be inappropriate for the roughest platforms. Based on these results, we examine the balance of wave breaking to frictional dissipation for rock platforms and find that friction is only significant for very rough, flat platforms during small wave conditions outside the surf zone.

1. Introduction

One of the longest standing debates in rocky coast geomorphology is whether subaerial weathering or wave processes dominate shore platform evolution (Kennedy et al., 2011), i.e., the 'wave versus weathering debate'. One approach to help resolve this issue is through the measurement of surf zone hydrodynamics to quantify wave energy dissipation, wave forces and wave-driven currents across shore platforms. For example, Stephenson and Kirk (2000) made wave height measurements across a quasi-horizontal platform in New Zealand and found that, despite the energetic offshore wave conditions, the amount of energy delivered to the platforms was very low with only 5 – 7 % of the wave energy at the seaward edge of the platform reaching the cliff foot; they concluded that wave erosion was not effective in this area. The quantification of wave energy levels across the shore platform is also relevant in assessing the delivery of wave energy to the cliff toe (Naylor et al., 2010), and for determining the likelihood of large boulders being moved by waves across the platform (Nott, 2003).

Shore platforms are (quasi-) horizontal or gently-sloping rock surfaces, generally centred around MSL and extending between spring high and spring low tidal level (Kennedy, 2015). They are abundant along energetic rocky coasts and are often backed by eroding cliffs, sometimes with a beach deposit present at the cliff-platform junction. The development of shore platforms is intrinsically linked to coastal cliff erosion (Trenhaile, 1987), and they have been described as erosional stumps left behind by a retreating sea cliff (Pethick, 1984).. Two shore platform types have been described (Sunamura, 1992): Type A platforms are characterised by a gently-sloping ($\tan\beta$ = 0.01 – 0.05) surface that extends beneath sea level without a marked break in slope, and are usually found in large tidal environments (mean spring tide range > 2 m); Type B platforms are characterised by a (quasi-)

horizontal surface fronted by a steep scarp (sometimes referred to as a low tide cliff) and typically occur in small tidal settings (mean spring tide range < 2 m).

Measurements have shown that shore platform gradient is positively correlated with tidal range (Trenhaile, 1999); however, it has recently been suggested that platform gradient may also be affected by the sea-level history (Dickson and Pentney 2012). The shore platform surface depends mainly on geological factors, such as lithology and the characteristics of the stratigraphic beds (thickness, strike, slip, etc.), and ranges from very smooth (similar to a sandy beach) to very rough (similar to a coral reef edge) (Trenhaile, 1987). Both the gradient and the roughness of shore platforms are expected to play key roles in driving nearshore dynamics through their effect on wave transformation processes, incident wave energy decay, wave set-up and infragravity wave generation.

Despite the recognised importance of wave processes in influencing shore platform dynamics and evolution (e.g., Dickson et al., 2013; Kennedy and Milkins, 2014), there is a paucity of appropriate process measurements made in these settings and even fewer studies in macrotidal environments. This represents a considerable time lag compared to nearshore research on sandy beaches, where wave data have been routinely collected since the 1980s (cf. Komar, 1998), and also compared to investigations of wave transformation process across coral reef platform (e.g., Brander et al., 2004; Lowe et al., 2005). The latter are rather similar to rocky shore platforms, both in terms of the gentle gradient (especially the Type B platforms) and the rough surface. Long term evolution of platforms has been addressed by Dickson et al., (2013) who challenges simplified steady-state equilibrium models that apply exponential decay, in wave height, and do not consider infragravity wave frequencies. This work links with that of Kennedy and Milkins, (2014) who address beach accumulation on platforms as a possible negative feedback to reduce cliff-retreat through increase wave dissipation.

A limited number of field data sets are available describing wave transformation across rocky shore platforms in micro-tidal settings. A common feature of these studies is the tidal modulation of the wave height and the depth limitation of the surf zone wave heights across the platform (Farrell et al., 2009; Marshall and Stephenson, 2011; Ogawa et al., 2011, 2015, 2016). The concept of a 'saturated surf zone' (Thornton and Guza, 1982) is well-demonstrated in each of these field investigations and concurrent with the dissipation of short-wave energy is the increase in the infragravity wave height (Beetham and Kench, 2011; Ogawa et al., 2015). The latter finding is potentially a very important geomorphic process, especially during energetic wave conditions (storms), because it is these waves that may dominate the water motion at the landward edge of the shore platform and provide the main force for cliff erosion and cliff-toe debris removal (Dickson et al., 2013).

A useful parameterisation of the wave conditions in the surf zone is the ratio of wave height H to water depth h. For mono-chromatic waves, this parameter is referred to as the breaker index γ and its value ranges from about 0.7 to 1.2. For random waves, H/h must be defined in statistical terms and usually the root-mean-square wave height H_{rms} or the significant wave height H_s is used. For consistency, all H/h values quoted in this paper are H_s/h, and values in the literature based on H_{rms} have been converted to H_s/h using $H_s = \sqrt{2}H_{rms}$. Original work on sandy beaches by Thornton and Guza (1982) suggested that H_s/h is constant in the surf zone with an upper-bound value of $H_s/h = 0.59$, and this value has also been found in subsequent work (Wright et al., 1982; King et al., 1990). However, field and laboratory studies of wave transformation processes have also found that H_s/h depends on wave steepness (Nairn, 1990), cross-shore position (Vincent, 1985) and beach gradient

106 (Sallenger and Holman, 1985; Masselink and Hegge, 1995). In particular, the latter dependency on
107 beach gradient is relevant for shore platforms: for example, assuming tanβ = 0 for a Type B platform
108 and tanβ = 0.03 for a Type A platform results in a value for H_s/h of 0.42 and 0.56, respectively,
109 according to Sallenger and Holman (1985), and 0.5 and 0.65, respectively, according to Masselink
110 and Hegge (1995). Based on field observations from three sandy beaches, Raubenheimer et al. (1996)
111 proposed the following equation that predicts H_s/h as a function of beach gradient tanβ, water depth h
112 and wave number k:

113 $$\frac{H_S}{h} = 0.19 + 1.05\frac{\tan\beta}{kh} \qquad \textbf{Eq. (1)}$$

114 where k is the local wave number given by $2\pi/L$, and where the wave length L is computed based on
115 the wave period derived from the incident-wave centroidal frequency. Care should be taken when
116 comparing H_s/h values between different studies due to the variety in methods used to derive H_s from
117 data (e.g., measurements based on wave staffs, pressure sensors and current meters; use of different
118 high- and low-frequency cut-offs, different methods for correcting for linear depth attenuation); for
119 example, Raubenheimer et al. (1996) uses a high-frequency cut-off of 0.18 Hz and does not correct
120 the remaining water level signal for depth attenuation. Additionally, H_s/h is also likely to depend on
121 offshore bathymetry that is not accounted for in the simple tanβ/kh parameterisation, e.g., the presence
122 of a sand bar.

123 Previous work on shore platforms has suggested values for H_s/h of 0.59 (Farrell et al., 2009), 0.4
124 (Ogawa et al., 2011) and 0.4 – 0.6 (Ogawa et al., 2015; depending on platform gradient). It is noted
125 that these H_s/h values are upper-bound values and not the result of least-squares analysis between H_s
126 and h for saturated surf zone conditions, such as was carried out to derive **Eq. (1)**. The notion of
127 identifying an upper-bound value for H_s/h stems from wave transformation studies across coral reef
128 platform where the aim is to identify the maximum wave condition that can occur for a given water
129 depth over the reef (e.g., Nelson, 1994; Hardy and Young, 1996). The parameter H_s/h is useful for
130 making an assessment of wave conditions as a function of water depth. For example, if H_s/h across a
131 shore platform is 0.5 and the water depth h at the landward extent of the platform and at the base of
132 the cliff is 2 m, then the waves impacting on the cliff are characterised by a significant wave height H_s
133 of 1 m. More specifically, however, H_s/h is related to the rate of incident wave energy dissipation in
134 the surf zone, which in turn controls radiation stress gradients, wave set-up and nearshore currents.

135 The ability to model the transformation of waves across the surf zone is clearly important, whether the
136 surf zone is on a sandy beach or a rocky shore platform. Analytical and numerical models use the
137 breaker index γ_s as an essential tuning/calibration parameter for computing surf zone wave
138 transformation and breaker-induced wave height decay (see Section 2). It has been established that
139 H_s/h is strongly dependent on the bed gradient tanβ (Sallenger and Holman, 1985; Masselink and
140 Hegge, 1995; Raubenheimer et al., 1996) and that steep surfaces are characterised by larger H_s/h
141 values than gently-sloping surfaces. What is unknown, however, is whether the roughness of the
142 surface over which the surf zone waves propagate plays a role in the wave transformation process and
143 directly affects the value of γ_s used in these models. According to Kobayashi and Wurjanto (1992),
144 incident wave energy dissipation due to bottom friction is negligible in the surf zone of sandy beaches;
145 however, Lowe et al. (2005) found that at the front of a coral reef, energy dissipation by bottom
146 friction was comparable to that by wave breaking under modal wave conditions, and even exceeded
147 breaking-induced dissipation under low wave conditions. These conflicting findings are easily

explained by the vastly different bed roughness values between sandy beaches and coral reefs. In terms of bed roughness, shore platforms can range from beaches to coral reefs, with their surfaces ranging from extremely smooth to extremely rough, and with vertical variability varying from several millimetres to up to a meter.

The aim of this paper is to investigate whether wave transformation processes on shore platforms are different from that on sandy beaches due to differences in bed roughness. Specifically, we hypothesise that rough shore platforms enhance incident wave dissipation by friction (as opposed to breaking) and may influence energy transfer to the infragravity band by changing wave energy gradients in the surf zone and lowering incident-band wave heights in the shoaling zone. The hypothesis will be tested by comparing H_s/h, as well as the amount of infragravity wave energy across five different shore platforms representing a range of bed roughness values and gradients, and comparing these values with those obtained from a sandy beach. The simple wave transformation model developed by Thornton and Guza (1983) will be used to help interpret and complement the field results, and is introduced and discussed in Section 2. The field sites and the methodology used to collect and analyse the data are described in Section 3. The results obtained in the field and derived from a numerical model are presented in Section 4 and 5, respectively, and the implications are discussed in Section 6.

2. Modelling wave transformation

The wave height across a mildly-sloping nearshore, whether a beach or a shore platform, can be predicted using the wave height transformation model of Thornton and Guza (1983), which is an extension of the earlier model of Battjes and Janssen (1978). Assuming straight and parallel contours, the energy flux balance is:

$$\frac{\partial E C_g}{\partial x} = -\langle \varepsilon_b \rangle - \langle \varepsilon_f \rangle \qquad \textbf{Eq. (2)}$$

where E is the energy density, C_g is the wave group velocity, x is the cross-shore coordinate, $\langle \varepsilon_b \rangle$ is breaker dissipation and $\langle \varepsilon_f \rangle$ is dissipation due to bed friction. The energy density and group velocity are calculated using the linear wave theory relationships:

$$E = \frac{1}{8}\rho g H_{rms}^2 \qquad \textbf{Eq. (3)}$$

$$C_g = \frac{C}{2}\left(1 + \frac{2kh}{\sinh 2kh}\right) \qquad \textbf{Eq. (4)}$$

where ρ is the density of sea water, g is the gravitational acceleration, H_{rms} is the root mean square wave height, k is the wave number corresponding to the peak frequency f_p of the wave spectrum and h is the local water depth. Thornton and Guza (1983) parameterise the rate of dissipation due to wave breaking as:

$$\langle \varepsilon_b \rangle = \frac{3\sqrt{\pi}}{16}\rho g B^3 f_p \frac{H_{rms}^5}{\gamma^2 h^3}\left[1 - \frac{1}{(1+(H_{rms}/\gamma h)^2)^{5/2}}\right] \qquad \textbf{Eq. (5)}$$

where B is an empirical breaker coefficient $O(1)$ for the case of fully developed bores (Thornton and Guza, 1982) and γ is the critical wave breaking parameter. The rate of dissipation due to bottom

friction is calculated by Thornton and Guza (1983) assuming quadratic bottom shear stress and parameterised as:

$$\langle \varepsilon_f \rangle = \rho C_f \frac{1}{16\sqrt{\pi}} \left[\frac{2\pi f_p H_{rms}}{\sinh kh} \right]^3 \qquad \textbf{Eq. (6)}$$

where C_f is the bottom drag coefficient.

The energy flux balance equation **Eq. (2)** is solved by substitution of the breaking wave dissipation **Eq. (5)** and bottom friction dissipation **Eq. (6)** functions, and numerically integrating over the cross-shore spatial domain using a simple forward-stepping scheme, where

$$EC_g|_2 = EC_g|_1 + \langle \varepsilon_b \rangle|_1 \Delta x + \langle \varepsilon_f \rangle|_1 \Delta x \qquad \textbf{Eq. (7)}$$

Starting from the offshore boundary (location 1), where $H_{rms,1}$ and f_p are known, the predicted quantities are obtained via **Eq. (7)**. $C_{g,1,2}$ and E_1 are computed using linear theory (**Eqs. (3)** and **(4)**) and the known values of $H_{rms,1}$, and h_1 and h_2. The rates of breaking wave and frictional dissipation (**Eqs. (5)** and **(6)**) are calculated, and E_2 and therefore $H_{rms,2}$ are then predicted.

The breaker coefficient B is generally taken as a constant (B = 1; e.g., Lowe et al., 2005); therefore, the wave height transformation according to the Thornton and Guza (1982) model is only determined by the two 'free' parameters γ and C_f, which, respectively, control the rate of dissipation through breaking and bottom friction. It is informative to analyse the effect of these parameters on wave transformation over a plane-sloping bed. Figure 1 shows the results of a number of simulations using **Eq. (7)** and a range of γ and C_f spanning values reported in the literature. The boundary conditions for the model runs are characterised by H_o = 0.6 m, T_p = 7.5 s and $\tan\beta$ = 0.02. Eight simulations were run with C_f fixed at 0.01 and γ varied from 0.35 to 0.7 (in 0.05 increments); the other eight simulations were run with γ held constant at 0.42 and C_f varied from 0.01 to 0.15 (in 0.02 increments).

Wave energy dissipation by breaking, parameterised by γ, exerts a strong control on the wave height transformation. Increasing γ allows larger waves to propagate and shoal closer to the shoreline before breaking. This increases the rate of breaker dissipation across a narrow cross-shore region and causes larger values of the local wave height to water depth ratio H/h. Wave energy dissipation by bed friction is controlled by the bed roughness, parameterised by a drag coefficient C_f. Increasing C_f enhances energy dissipation and opposes the increase in wave height during the shoaling process. Energy dissipation due to friction is generally less than by wave breaking, even for the largest C_f values, and is mainly observed outside the surf zone. There is a weak influence of C_f on the local H/h with the largest H/h values associated with the smoothest bed (smallest C_f). Overall, these model results suggest that γ exerts the primary control over wave height transformation across the nearshore in the surf zone across the typical geometry of Type A rock shore platform (1/50 slope), but that dissipation via bottom friction will cause a reduction in wave heights (or less shoaling) seaward of the surf zone. By optimising predicted cross-shore variation in wave height with field observations, the values for the two parameters γ and C_f can be obtained. In Section 4, shoaling wave data will be used to optimise C_f for the different field sites, whereas surf zone data will provide the means to optimise γ.

3. Methodology

3.1. Field sites

Five field deployments were undertaken during the winter months of 2014 – 2015 at four UK and one Irish location with well-developed shore platform morphology (Figure 2), and all representing relatively energetic and large tidal range settings. The sites were Doolin in Ireland (DOL; Figure 2a), Freshwater West in Pembrokeshire, Wales (FWR and FWB, representing both platform and sandy beach sites, respectively; Figure 2b), Lilstock in Somerset, England (LST; Figure 2c), Hartland Quay in north Devon, England (HLQ; Figure 2d), and Portwrinkle in south Cornwall, England (PTW; Figure 2e). These sites, excluding FWR and FWB, have been described by Poate et al. (2016) and site details are summarised in Table 1.

Figure 3 shows the cross-shore profiles of all sites and indicates that a range of platform morphologies are represented in the data. The Doolin platform is relatively narrow (x = 160 m), has the steepest gradient ($\tan\beta$ = 0.031) and has a rather stepped morphology due to the limestone beds. The Freshwater West site was chosen to complement the four other deployments as it provided an ideal opportunity to measure two parallel sensor arrays, one across the relatively flat shore platform (FWR; $\tan\beta$ = 0.018) and one across the flat sandy beach (FWB; $\tan\beta$ = 0.011), to compare bed roughness effects on wave transformation processes under identical forcing. The Lilstock platform experiences the largest tide range (MSR = 10.7 m) and represents the widest platform (x = 325 m), whilst the Hartland Quay and Portwrinkle platforms are both relatively narrow (x = 140 m and x = 180 m, respectively) and steep ($\tan\beta$ = 0.030 and $\tan\beta$ = 0.028, respectively) platforms. All platforms have some degree of gravel-cobble beach deposit at their landward end, but these are particularly well developed at Hartland Quay and Lilstock. The roughness of the shore platform surfaces will be discussed in Section 4.1, but it can already be observed in Figure 3 that the platforms at Portwrinkle and Lilstock represent the roughest and smoothest surfaces, respectively.

3.2. Morphological data

Platform morphology was surveyed using RTK-GPS to obtain representative cross-sections through the instrument arrays (cf. Figure 3). Survey points were taken at least every metre, capturing all significant irregularities and slope breaks. Cross- and alongshore platform variability was mapped at high spatial resolution (3.1 mm at 10 m distance) using a Leica P20 terrestrial laser scanner. A 40-m wide strip of the platform was scanned using 6 – 12 scan positions centred around the instrument array. A digital elevation model (DEM) of the platforms was obtained by interpolating the high-resolution scan onto a regular 0.1 x 0.1 m grid.

The quantification of surface roughness is essential to determine the influence of the platform roughness on wave transformation processes. Two simple measures were used based on 1x1 m square tiles of the platform DEM. The first measure is, analogous to computing the height of wave ripples (Nielsen, 1992), four times the standard deviation associated within the square tiles ($k_\sigma = 4\sigma_z$) and has units of m. Lowe et al. (2005) calculated k_σ using observations of wave dissipation across a coral reef environment, and found typical values of k_σ = 0.16 m, which compared very well with measurements of the roughness. The second measure is the rugosity (k_R) defined as A_r/A_a,-1 where A_r is the actual surface area of the square tiles and A_a is the geometric surface area (1 m^2). Rugosity is widely used in coral reef studies because it is relatively easy to determine in the field and k_R = 0 (1) for a smooth

(infinitely rough) surface. The estimates of the roughness parameters k_σ and k_R were alongshore-averaged across the 40-m wide strip to obtain the cross-shore variability in bed roughness.

3.3. Hydrodynamic data

Water levels were measured using a shore-normal array of up to fifteen RBR solo D-Wave pressure transducers (PTs), individually housed within steel tubes and fixed to the bedrock with 10 – 15 m spacing. The PTs covered the full spring intertidal zone of the sites to capture shoaling, wave breaking, surf zone and swash conditions, and the deployment strategy was kept consistent to aid comparison between sites. The field deployments lasted 8 – 13 tides with sensors sampling continuously at 8 Hz. Video cameras were used to log the periods of platform inundation during daylight hours. Individual image files were recorded at 4 Hz and used during subsequent processing to identify regions of breaking waves with reference to the pressure sensor locations.

A barometric pressure compensation (determined as the pressure recorded by the (exposed) sensors during each low tide) was used to convert absolute pressure recorded by the PTs to hydrostatic pressure. The dynamic pressure signal was corrected for depth attenuation using a local approximation approach (Nielsen, 1989) and the water depth (h) required for this approach was derived using a 10-minute moving average filter.

All data analysis was conducted using 20-min data segments (N = 9600); a compromise between limiting tidal non-stationarity in macrotidal settings and having sufficient data length to obtain representative statistical parameters. Spectra were computed using Welch's segment-averaging approach with 8 Hanning-tapered segments overlapped by 50%, proving 16 degrees of freedom. The spectral energy was partitioned into infragravity- and incident-wave energy, with the cut-off frequency separating these two frequency bands determined for each site and for each tide using the high tide wave spectrum from the seaward-most PT. If a spectral valley was present, the frequency associated with the minimum spectral energy was selected as the cut-off; in the absence of a clear spectral valley, a fixed cut-off value of 0.047 Hz was used. No high frequency cut-off was applied. Using the array method of Gaillard et al. (1980), the wave spectra were redefined into incoming and outgoing components, from which the infragravity and incident wave heights ($H_{s,inf}$ and $H_{s,inc}$) were computed as four times the square root of the total spectral energy summed over the relative frequency bands. The spectral mean wave period was derived from the spectral moments (T_{spec} = m_1/m_0). Additional wave parameters computed for the 20-min data segments include the wave power or energy flux ($P = EC_g$) calculated according to linear wave theory (**Eqs. (3)** and **(4)**), the wave skewness was calculated from the water surface elevation time series ($skewness = \sum(n - \bar{n})^3/\sigma n^{1.5}$) where n = water surface elevation, $\bar{n}$ = average water surface elevation and σ = variance, while the asymmetry is the skewness of the derivative of the water surface.

To determine the contribution of wave breaking and bed friction to wave energy dissipation, and assess the role of bed roughness in these processes, it is essential to know whether data are from the surf zone or the shoaling wave zone. Additionally, knowledge of the breaker wave height (H_b) and breaker depth (h_b) are important for normalising the position of the data relative to the breakpoint. For each 20-min data segment, the cross-shore variation in the wave height was used to identify H_b and h_b from the maximum wave height in the cross-shore array, with visual calibration performed through the video images whenever possible (Figure 4). If a clear spatial peak in the wave height was not

discernible, usually because the surf zone extended beyond the seaward-most pressure sensor (due to large wave heights and/or low tide level), that data segment was not used for determining the breaker conditions. Then, for every tide, the significant breaker height and the breaker depth were averaged using all data segments for which the breaker conditions could be determined. Due to the very strong tidal currents in the Bristol Channnel, the wave conditions at Lilstock exhibit a very pronounced diurnal inequality with the rising tide wave conditions much more energetic than the falling tide conditons; the falling tide data for Lilstock were removed from the analysis.

4. Results

4.1. Platform roughness

Figure 5 presents the de-trended DEMs of all study sites, including the sandy beach, and the alongshore-averaged bed roughness parameters k_σ and k_R. The scaling for the DEMs is the same for all sites and it is evident that the surfaces of the shore platforms are highly variable, with Portwrinkle clearly the roughest platform and Lilstock the smoothest. The sandy beach at Freshwater West represents, not surprisingly, by far the smoothest surface. In addition to providing useful insight to the main roughness elements, the DEMs also highlight the geological bedding, which is almost shore-perpendicular at Hartland Quay, oblique to the shore at Freshwater West, almost shore-parallel at Doolin and Lilstock, and complex at Portwrinkle. Faults also contribute to roughness (e.g., Hartland Quay, Portwrinkle).

The visual difference in platform roughness is well quantified by the alongshore-averaged roughness parameters plotted in Figure 5. The roughest platform (Portwrinkle) has typical values for k_σ and k_R of 0.3 m and 0.2, respectively, the smoothest platform (Lilstock) has values 0.1 m and 0.05, respectively, and the sandy beach 0.01 m and 0.01, respectively. For all sites, the bed roughness parameters do not vary much across the profile and can be characterised by a single value (cross-platform average): variability between the sites is generally greater than variability within the sites. It is noted that the values of the roughness parameters k_R and especially k_σ increase with the grid size of the DEM. A grid size of 1 m was adopted for all sites; therefore, the roughness values are directly comparable with each other, but not necessarily with that of other studies.

4.2. Wave conditions

Considerable variability in the forcing wave conditions was experienced during all field experiments, with offshore significant breaker heights ranging from 0.5 m to 3 m (Figure 6). At all sites, energetic conditions with breaker heights exceeding 1.5 m occurred for multiple tidal cycles, and breaker conditions were generally less energetic than the offshore wave conditions. The largest breaking waves were encountered at Freshwater West (H_b = 1.8 – 2.4 m) and the calmest conditions occurred at Portwrinkle (H_b = 0.7 – 1.0 m).

As detailed in Section 3.3, all data were inspected to identify breaker conditions (H_b and h_b) and tide-averaged H_b/h_b was found to increase with the breaker wave height. It is not quite clear why this is the case (possibly wave steepness dependency), but because of the large observed variability in H_b/h_b, with values ranging between 0.25 and 0.6, a tide and site-specific value for H_b/h_b is used. This value

was used in combination with the local water depth (h), to obtain the relative surf zone position (h/h_b), where $h/h_b = 0$ denotes the shoreline and $h/h_b = 1$ represents the start of the surf zone.

4.3. Incident wave height

During all tides and at all sites, the cross-shore variability in the incident wave height measured by the PT array displayed the well-established 'saturated' signature in the surf zone with $H_{s,inc}$ decreasing with decreasing h (Figure 7). Outside the surf zone, $H_{s,inc}$ increases up to the breakpoint due to wave shoaling for most data runs. The ratio $H_{s,inc}/h$ generally increases in the landward direction, both inside and outside the surf zone, in line with predictions according to the Thornton and Guza (1983) model (cf. Figure 1).

The $H_{s,inc}/h$ values for all data are distributed into class bins and plotted versus the normalised platform/beach slope ($\tan\beta/kh$) and compared to **Eq. (1)** in Figure 8. Although the trends in the field data are similar to those predicted by **Eq. (1)**, the observed $H_{s,inc}/h$ values are consistently higher than predicted. This is attributed to differences in the way the raw pressure data were processed: Raubenheimer et al. (1996) removed frequencies > 0.18 Hz from the analysis and did not correct the pressure signal for depth attenuation (an approach that was considered inappropriate for the range of wave periods represented in the current data set and one that would have led to a systematic under-prediction of the data collected under relatively-short period wave conditions). Application of the 0.18-Hz filter by Raubenheimer et al. (1996) is expected to have significantly reduced the incident wave energy and H_s, and therefore the H_{sinc}/h values. The key observation from Figure 8 is that for most sites the H_{sinc}/h values are similar with the variability in H_{sinc}/h explained reasonably well by the platform/beach gradient and the non-dimensional water depth, parameterised by $\tan\beta/kh$. Despite considerable variability in the roughness of the platform surfaces (and sandy beach), it is not apparent that bed roughness plays a significant role in affecting H_{sinc}/h. An exception would appear to be at Portwrinkle, which is the roughest platform, where the H_{sinc}/h values are smallest and are closest to the predictions by **Eq. (1)** for the seaward-most data segments (smallest values of $\tan\beta/kh$) and less than the predictions for the landward-most data segments (largest values of $\tan\beta/kh$).

4.4. Wave shape

Transformation in wave shape is explored in Figure 9, where wave skewness (A_{skew}) and wave asymmetry (A_{asym}), computed using the Hilbert transform (cf. Ruessink et al. 2012), are plotted against the normalised surf zone position (h/h_b) for each 20-minute data burst. For three of the sites (DOL, FWR, FWB), the skewness increases steadily up to the breakpoint ($h/h_b = 1$) and then decreases towards the shoreline. At HLQ and PTW, the peak in skewness occurs around the mid-surf zone position ($h/h_b = 0.4 - 0.6$), after which A_{skew} remains constant, whereas at LST, skewness is more or less constant across the entire surf zone. The trends in the wave asymmetry is much more consistent across all sites and A_{asym} becomes increasingly negative (more asymmetric) towards the shore.

The Ursell number (Ur), calculated following Doering and Bowen (1995), gives an indication of the nonlinearity of the waves across the platform at each site, where larger Ur values represent stronger non-linear effects:

$$Ur = \frac{3}{4}\frac{a_w k}{(kh)^3} \qquad \textbf{Eq. (8)}$$

with $a_w = 0.5H_s$. Figure 10 shows the wave skewness and wave asymmetry as a function of the Ursell number. For DOL, FWR and FWB, the skewness values increase from close to zero for low Ursell values ($Ur < 0.4$) and peak at $A_{skew} = 1 - 1.5$ around $Ur = 1 - 2$. For LST, HLQ and PTW there is no clear maximum in skewness and A_{skew} remains more or less constant at $A_{skew} = 0.5 - 1$ for $Ur > 2$. Wave asymmetry is near-zero for $Ur < 0.5$ and becomes increasingly negative (increasingly asymmetric in shape) with increasing Ur values, reaching maximum values near the shoreline ($A_{asym} < -0.5$).

Our results are compared with the predictions of Ruessink et al. (2012):

$$A_{skew} = B\cos(\frac{\psi\pi}{180}) \quad \textbf{Eq. (9)}$$

$$A_{asym} = B\sin(\frac{\psi\pi}{180}) \quad \textbf{Eq. (10)}$$

where

$$B = P_1 + \frac{P_2 - P_1}{1+exp\frac{P_3 - logUr}{P_4}} \quad \textbf{Eq. (11)}$$

$$\psi = 90^\circ + 90^\circ\tanh(\frac{P_5}{Ur^{P_6}}) \quad \textbf{Eq. (12)}$$

and $P_1 = 0$, $P_2 = 0.857 \pm 0.016$, $P_3 = 0.471 \pm 0.025$, $P_4 = 0.297 \pm 0.021$, $P_5 = 0.815 \pm 0.055$, $P_6 = 0.672 \pm 0.073$, (Figure 10). Skewness at DOL, FWR and FWB is consistently under-predicted, whereas at LST, HLQ and PTW there is a reasonable fit for $Ur < 2$ but also under-prediction for greater Ur values. The asymmetry observations at DOL, FWR and FWB match the Ruessink et al. (2012) predictions quite well across the full range of Ur values, but at LST, HLQ and PTW the A_{asym} values are under-predicted for $Ur > 1$. In summary, in comparison with the predictions of Ruessink et al. (2012), which were derived from data collected on sandy beaches, the waves propagating across the shore platforms appear to have been more skewed at DOL, FWR and FWB indicating enhanced shoaling, and less asymmetric at LST, HLQ and PTW suggestive of not fully-developed asymmetric bores.

4.5. Infragravity wave height

Development of infragravity waves (wave height and percentage energy) across the platforms is expressed against the normalised surf zone position (h/h_b) in Figure 11. Incoming infragravity wave heights are greatest at DOL, FWR and FWB ($H_{s,inf} = 0.5 - 1$ m), while LST and HLQ have the smallest waves ($H_{s,inf} = 0.1 - 0.3$ m). In the landward direction, $H_{s,inf}$ increases for DOL, decreases for FWR and FWB, and is relatively constant for the other sites. The decrease at FWR and FWB reflects the dissipation of infragravity energy, observed by De Bakker et al. (2016), where the focus is on incoming infragravity heights not heights as a percentage of the total. At all sites, the proportion of infragravity energy increases in the landward direction. LST stands out as having the smallest proportion of infragravity energy with only a small rise after the breakpoint ($h/h_b = 1$).

Inch et al. (2016), who worked on a low-gradient ($\tan\beta = 0.015$) and high-energy ($H_s = 1 - 4$ m) dissipative beach, showed that the infragravity wave height could be scaled by an incident wave

power factor $H_o^2T_p$ according to H_{inf} = 0.004$H_o^2T_p$+0.2, where H_{inf} is the tidally-averaged total infragravity wave heights (H_{inf} averaged over each tidal cycle) measured where 0 < *h/hb* < 0.33. Recorded values of H_{inf} are compared with $H_o^2T_p$ for each site (**Error! Reference source not found.**) and, with the exception of DOL, the equation proposed by Inch et al. (2016), over-predicts the infragravity wave height for all sites.

4.6. Bulk statistics

For overall comparison between the sites, mid-surf zone position bulk parameters (total wave signals, averaged over all PTs where h/h_b = 0.45 to 0.55) for $H_{s,inc}/h$, A_{skew}, A_{asym} and *%Ig* are presented in Figure 13 with their corresponding 95 % confidence intervals. Across all of the parameters and sites, there are a number of statistically significant differences (indicated by non-overlapping CI's), but few clear trends exist for any one location and there are no sites that consistently score highest/lowest. In terms of similarity, the data can be grouped as follows: (1) DOL and FWR have the highest $H_{s,inc}/h$ and *%Ig* values and are the most non-linear (both in terms of skewness and asymmetry; (2) LST, HLQ and PTW are characterised by the lowest $H_{s,inc}/h$ and *%Ig* values, and are the least non-linear; and (3) FWB falls very much between these two groups in all aspects, except for $H_{s,inc}/h$, where it is characterised by the lowest value, although this could be due to a limited number of measurements from the inner-surf zone region. The link between the bulk parameters and platform roughness will be addressed within the discussion.

A strong association appears to be present between the proportion of infragravity energy (*%Ig*) and the wave asymmetry (A_{asym}). DOL and FWR have the largest *%Ig* compared to the other sites and are characterised by the most asymmetric (pitched-forward) wave form; the sites with the least asymmetric surf zone waves (LST, HLQ and PTW) were characterised by the lowest *%Ig* values. Greater values of A_{asym} suggests enhanced bore development and more intense short-wave dissipation.

5. Numerical Model

The purpose of the energy flux model (**Eq. 2**) is to support the field observations by exploring the parameter space of γ and C_f relative to platform roughness. The model is initialised at the seaward boundary (x = 0 m) using observations from the most offshore PT. A normalised cross-shore grid spacing of $\Delta x' = \Delta x/T_p\sqrt{gH_o} = 0.01$, where Δx is the dimensional grid size, is used and the profile smoothed with a 6-m moving-average filter (determined using a convergence test) to minimise small-scale steps in the bathymetry caused by the geometry of individual rock elements. First, the model is calibrated for the free parameters γ and C_f which control the dissipation by wave breaking and friction, respectively.

Seaward of the surf zone, the dissipation of short wave energy is dominated by bottom friction and is therefore principally controlled by the bed roughness; this zone can therefore be used to calibrate C_f. Data from four tides from each field site (excluding FWB where the PT array was too short to permit reliable model optimisation) were used to calibrate the model, totalling approximately 750 model simulations. To calibrate C_f, we only used data recorded from seaward of the surf zone .A strict a-priori assumption of the breaker criterion γ ($H_{s,inc}/h$) for the region seaward of the surf zone was determined by a visual inspection of the data bursts from each tide (typically $H_{s,inc}/h$ = 0.28 – 0.42) as described in Section 3.3, identifying those PTs which were very clearly located seaward of the surf zone and where dissipation must be solely due to bottom friction. The model was run for each of these

tides over a range of C_f and with γ set to 0.42, a typical value from the existing literature (e.g., Thornton and Guza, 1983). The optimum value for C_f was determined by minimising error estimates between the observed and modelled wave heights across the region seaward of the surf zone.

To quantify the model error, the absolute root-mean-square error ϵ_{abs} and relative bias ϵ_{bias} were computed by comparing the incident wave height $H_{s,inc}$ obtained from the measurements (M) with the computed H_s (C) at each PT location (i) and for each 10-minute burst (t), and where $|-|$ indicates the modulus and $\langle - \rangle$ the mean, respectively:

$$\epsilon_{abs} = \sqrt{\langle C_{(i,t)} - M_{(i,t)} \rangle^2} \quad \textbf{Eq. (13)}$$

$$\epsilon_{bias} = \sqrt{\langle C_{(i,t)} - M_{(i,t)} \rangle^2} / \max_{0 \to \infty} \left(\epsilon_{abs}, \left| \langle M_{(i,t)} \rangle \right| \right) \quad \textbf{Eq. (14)}$$

Values of ϵ_{abs} and ϵ_{bias} tending to zero indicate higher model performance. The most offshore PT was excluded from the calibration, since data from this location are used as the seaward boundary forcing for the model, and are thus not independent. This calibration was repeated for all field sites and the optimum C_f for each site was determined by minimising the rms and bias errors for every burst within each tide and computing the mean C_f by averaging the rms and bias errors (Figure 14). DOL, HLQ and PTW display parabolic curves of the distribution of the rms error for C_f, with the optimum C_f indicated by the minima. However, for FWR and LST the error curves asymptotically tend towards zero, indicating an effective model C_f of zero. The distribution of the bias displays a similar pattern across the field sites, and indicates that the shoaling wave heights at FWR and LST are under-predicted, which explains why the optimisation is driving C_f towards zero at these sites.

Inside the surf zone, however, wave energy is dissipated by both bottom friction and wave breaking. The model was calibrated for γ by optimising model performance for PTs determined to be within the surf zone, with C_f set to the value determined above for the region seawards of the surf zone. As for C_f above, the optimum γ for each field site was determined as the mean γ of the combined rms and bias errors for each tide (Figure 15). The results for the calibration of γ display clear parabolic curves for the rms errors at all sites except PTW, which tends to increase towards larger values of γ, and the results are consistent between rms and bias errors.

Example model outputs for each platform are compared to field observations in Figure 16. Absolute root mean square errors for H_s are $O(10^{-2})$m based on the four calibration tides at all platforms, and qualitatively the model performance is very good at all cross-shore locations, except at the very shallow landward-most PT at DOL and FWR, which experience significant wave reflection, wave set-up and non-linear processes not included in the simple model, and the mid-surf zone region at PTW. Rates of wave energy dissipation are also well predicted and reveal that frictional dissipation appears to be negligible at all sites except PTW. At PTW, frictional dissipation is observed to increase moving landwards from the shoaling wave to surf zone, presumably as wave orbital velocities increase under the breaking waves, but breaker dissipation remains the dominant in the surf zone. It is noteworthy that there are several large spikes of predicted dissipation (i.e., at DOL and PTW) that are not observed in the field observations. These result from instantaneous model dissipation over step changes in profile bathymetry to which the waves observed in the field do not appear to immediately respond and it results in the overall model error being greatest for PTW. A landward increase in $H_{s,inc}/h$ (typically 0.4 – 1.0) is observed for both the field and model data. This is consistent with the observations of Ogawa et al. (2011) and is the expected model behaviour when wave breaking is the

dominant mode of dissipation (Figure 1). It is well predicted by the model at all sites except HLQ, which displays a consistent over-prediction at the landward end of the platform; it is unclear why this is the case.

The dissipation parameters determined via the optimisation of the energy flux model, averaged over the four tides at each field site, are presented in Table 2. The combined estimates of γ and C_f from the model provide an indication of the relative importance of short-wave dissipation by bottom friction and by wave breaking over the rock platforms. The optimised γ_s range from 0.51 at DOL to 0.93 at PTW, which extends from the upper range typically reported from sandy beaches (~0.5 – 0.64) to significantly higher values. The optimised C_f are highly variable, ranging from $O(10^{-4})$ at FWR and LST to $O(10^{-1})$ at PTW. Qualitatively, the C_f values for LST (smoothest) and PTW (roughest) are consistent with the observed platform roughness length-scales k_σ and k_R, but it is unclear why it is so low for FWR, the second roughest site. The mean ratio of frictional to breaker dissipation $\langle \varepsilon_f / \varepsilon_b \rangle$ at the mid-surf zone position ($0.45 \geq h/h_b \geq 0.55$) for all tides examined is typically < 0.15 (Table 2); only at PTW does friction dominate where $\langle \varepsilon_f / \varepsilon_b \rangle = 3.82$.

6. Discussion

6.1 Analysis of field data

Field data collected from five sloping (Type A) rock shore platforms (Sunamura, 1992) and one intertidal beach were used to study wave transformation processes across the intertidal surfaces and specifically address the role of surface roughness on wave transformation. Due to the different lithology and bedding types, the five shore platforms represent a range in surface gradient and roughness. The platforms at Freshwater West (FWR) and Lilstock (LST) are relatively gently-sloping ($\tan\beta$ = 0.018 and 0.021, respectively) and the steeper platforms are present at Portwrinkle (PTW), Hartland Quay (HLQ), and Doolin (DOL) ($\tan\beta$ = 0.028, 0.30, and 0.31, respectively). LST represents the smoothest surface (k_R = 0.015) and the roughest platform is at PTW (k_R = 0.090). The beach site FRB is characterised by the gentlest gradient ($\tan\beta$ = 0.011) and the smoothest surface (k_R = 0.002). During the fieldwork the different sites experienced varying wave and tidal conditions, with PTW and FWR representing the smallest and largest waves (H_b = 0.7 – 1.0 m and H_b = 1.7 – 2.5 m, respectively), and DOL and LST experiencing the smallest and largest tides (MSR = 4.2 m and MSR = 10.7 m, respectively). A large number of pressure sensors (12 – 15) were deployed in a single transect across each shore platform and data were collected over 8 – 13 tides. This dataset represents the most extensive ever collected on rocky shore platforms, both in terms of the range of environmental conditions experienced, and the duration and spatial resolution of the measurements. It also represents the only wave transformation data set so far collected on Type A platforms, as all previous studies have been conducted on sub-horizontal Type B platforms.

In agreement with all previous studies of wave transformation across shore platforms, wave energy is strongly tidally-modulated and is depth-limited (i.e., saturated) across the inner part of the intertidal region (e.g., Farrell et al., 2009; Marshall and Stephenson, 2011; Ogawa et al., 2011). Additionally, the relative contribution of infragravity energy to the total wave energy content in the surf zone increases in a landward direction (cf., Beetham and Kench, 2011; Ogawa et al., 2015). We also demonstrate that the absolute infragravity energy level, quantified by the incoming infragravity wave height, decreases in the landward direction. The intertidal shore platforms, therefore, represent effective dissipaters of both incident and infragravity energy. As the waves propagate and dissipate across the platform, there are also systematic changes in the wave shape: wave skewness increases up

to the seaward extend of the surf zone and then decreases (DOL, FWR, FWB) or stays more or less constant (HLQ, LST, PTW), and at all sites the wave asymmetry becomes increasingly negative in the landward direction indicating the presence of turbulent and forward-pitching bores, indicative of continuous wave breaking.

The local wave height to water depth ratios $H_{s,inc}/h$ calculated here over the shore platforms compare favourably with those reported where wave breaking is the dominant form of dissipation over sandy beaches (Raubenheimer et al., 1996), near-horizontal rock platforms (Ogawa et al., 2011) and the fore reef of coral reefs (Vetter et al., 2010). Significantly, the consistent landwards increase in $H_{s,inc}/h$ indicates that dissipation by wave breaking is a continuous process across the platforms, confirmed by the observed landward increase in negative wave asymmetry, and that at any cross-shore location there is a combination of breaking and broken waves. This contrasts to observations across similarly rough (or rougher) coral reefs platforms, where the initial peak in $H_{s,inc}/h$ observed as waves break on the steep fore reef is followed by a decrease in $H_{s,inc}/h$ as energy dissipation becomes dominated by frictional drag with no breaking over the sub-horizontal reef flat (Lowe et al., 2005; Vetter et al., 2010, Rodgers et al., 2016). This difference occurs because the shore platforms studied here have relatively steep and near-constant planar slopes, whereas on coral reefs there is a clear distinction between the steeply-sloping fore reef and the sub-horizontal reef platform. As such, the morphology of coral reefs is rather similar to that of Type B shore platforms; therefore, care should be taken in extrapolating the present findings derived from Type A platforms to Type B platforms.

The aim of this paper is to investigate whether wave transformation processes on shore platforms are different from that on sandy beaches due to differences in bed roughness. The approach has been to compare observed data trends in terms of relative wave height ($H_{s,inc}/h$), wave skewness (A_{skew}), wave asymmetry (A_{asym}) and incoming infragravity wave height ($H_{s,inf}$) between the different platforms and with expressions related to these parameters from the literature derived from sandy beaches. The systematic landwards increase in $H_{s,inc}/h$ was linked to the normalised slope $\tan\beta/kh$ using **Eq. 1** based on Raubenheimer et al. (1996), which combines the non-dimensional water depth kh with the bed gradient $\tan\beta$, and which provides a good description of the data (accounting for under-prediction due to the difference in data filtering prior to analysis; cf., Section **4.3**). The dependence of $H_{s,inc}/h$ on $\tan\beta$ is also evident when comparing across the different platform sites, with the steeper platforms DOL, HLQ, PTW displaying larger surf zone values of H_s/h than the flatter platforms LST and FWR and particularly the beach FWB. This is consistent with studies on sandy beaches (e.g., Sallenger and Holman, 1985; Masselink and Hegge, 1996). No obvious control of the platform roughness on $H_{s,inc}/h$ could be discerned. The development of wave non-linearity (skewness and asymmetry) was compared with formulations (**Eqs. 9 – 12**) suggested by Ruessink et al. (2012). The qualitative trends in the data, as a function of the Ursell Number (Ur; **Eq. 8**), are well represented by these equations, specifically the increase then decrease in wave skewness, which peaks at $Ur = 1 – 2$, and the progressive increase in negative wave asymmetry with decreasing Ur. The most pitched-forward surf zone waves (most negative A_{asym}) and the highest skewness values were observed at the sites which experienced the most energetic wave conditions (DOL, FWR, FWB), and no obvious influence of platform roughness on wave shape was observed. When compared with sandy beaches, the spatial trends in wave shape is similar, which would suggest the role of roughness is not significant.

Following the work of Inch et al. (2016), the total infragravity wave height (H_{inf}), where $0< h/hb <0.33$, was related to a wave power parameter ($H_o^2T_p$). With the exception of DOL for some tides, the observed values of H_{inf} are consistently over-predicted by the formulation of Inch et al. (2016). We attribute this to enhanced friction imparted on the infragravity wave motion by the rough platform

surfaces, leading to suppressed infragravity wave energy in the (inner) surf zone. This suggestion is supported by McCall et al. (2017) who used the current data set and the XBeach numerical model to investigate the relationship between the drag coefficient (used for parameterising friction for steady currents and infragravity wave motion) and the platform roughness. They found that if a smoothed rock platform profile was used, the drag coefficient required to provide the best agreement between observed and modelled infragravity wave energy levels increased with platform roughness.

In a final attempt to identify a demonstrable influence of platform roughness on wave transformation parameters, average values for a range of variables were computed for each of the platforms. The 'independent' variables selected are wave power (H_b^2T; averaged over all tides with data), platform gradient ($\tan\beta$) and platform roughness (k_σ and k_R), and are listed in Table **1**. The 'dependent' variables are relative wave height ($H_{s,inc}/h$), percentage incoming infragravity wave height ($\%H_{s,inf}$), wave skewness (A_{skew}) and wave asymmetry (A_{asym}). The dependent variables were averaged for each of the sites, but only for data from the mid-surf zone position (h/h_b = 0.45 – 0.55), and are shown in Figure **13**. A correlation matrix was constructed (not shown), and only four correlations were statistically significant at a level higher than 0.1. Strong correlations were obtained between the different wave parameters: wave skewness was correlated with the breaking wave power (r = 0.88; p = 0.02), whereas wave asymmetry was correlated with the percentage of incoming infragravity energy (r = -0.85; p = 0.03). Finally, a weak correlation was found between the bed gradient and the relative wave height (r = 0.72; p = 0.10), supporting previous work on sandy beaches (e.g., Raubenheimer et al., 1996). Most importantly, none of the dependent variables are correlated to the platform roughness.

6.2 Numerical modelling

The simple numerical model of Thornton and Guza (1983) was used to support the field observations and investigate the dissipation of the incident wave energy across the platforms by wave breaking and bottom friction, parameterised by γ_s and C_f, respectively. The optimised values for the model breaker criteria γ_s (0.51 – 0.93, Table 2) are larger than the observed bulk mid-surf zone values of $H_{s,inc}/h$ (Figure 13a) for all sites except DOL, but encouragingly fall between the range of values reported in the literature for sandy beaches (0.4 – 0.59) (Thornton and Guza, 1983; Sallenger and Holman, 1985; Raubenheimer et al., 1996) and coral reefs (0.59 – 1.15) (Lowe et al., 2005; Vetter et al., 2010; Péquignet et al., 2011). The result of the calibration for C_f is less clear, since, although the optimum value of C_f at LST (0.005), DOL (0.05), HLQ (0.049) and PTW (0.34) reflect the increasing hydraulic roughness of these platforms, the range of C_f spans two orders of magnitude. C_f was also estimated from the data for the tides used in the model calibration by regressing the measured rate of dissipation **Eq. (2)** across all adjacent PT pairs in the region seaward of the breakers against **Eq. (6),** where C_f is the regression coefficient (e.g., Wright et al., 1982). A large amount of scatter was observed in the data that was attributed to strongly shoaling waves, but statistically significant ($p < 0.05$) estimates of $C_f \approx 0.1$ were obtained for DOL, LST and PTW, which fall within the range of values obtained from the model calibration. Whilst this large range leads us to question how representative the calibrated values of C_f are, it is encouraging that except for LST (where C_f is very small), the values fall within the region between sandy beaches (0.01, e.g., Thornton and Guza, 1983) and coral reefs (0.16, 0.22 and 1.8, Lowe et al., 2005; Falter et al., 2004; Monismith et al., 2015); therefore, we also compare our calibrated values of C_f with the empirical wave friction model of Nielsen (1992) to gain further insight.

Nielsen (1992) predicts the wave friction factor f_w for rough turbulent boundary layers as a function of the ratio of the near-bed horizontal wave orbital amplitude A_b to the hydraulic roughness length-scale k_w (e.g., Jonsson, 1966; Swart, 1974; Madsen, 1994)

627 $$f_w = \exp\left[5.5\left(\frac{A_b}{k_w}\right)^{-0.2} - 6.3\right].$$ **Eq. (17)**

628 The value of k_w is usually specified as a function of the grain diameter D, where $k_w = 2D$ (Nielsen,
629 1992). To be consistent with the definition in **Eq. (17)**, $D \approx 2\sigma_r$, where σ_r is the roughness amplitude
630 and $k_w = 4\sigma_r$ (e.g., Lowe et al., 2005). Applying **Eq. (17)** to the roughness estimated using the
631 terrestrial laser scanner, $k_w \equiv k_\sigma$ (Figure 5; Table 1), allows a comparison with the predicted drag
632 coefficient C_f derived from the numerical model through the relationship $f_w = 2C_f$. The mean drag
633 coefficients computed over the four model optimisation tides for all of the platforms using **Eq. (17)**
634 are $O(10^{-2})$ with the smallest value associated with the smoothest platform (LST, 0.0225) and the
635 largest with the roughest (PTW, 0.069). Comparing these empirical estimates with those determined
636 via the numerical model optimisation shows that the trends in C_f are well replicated when FWR is
637 excluded, and that for our middle range of platforms DOL and HLQ ($\tan\beta \sim 0.03$, $k_\sigma \sim 0.02$), the
638 empirical and numerical estimates are in close agreement. For the roughest platform PTW, C_f is
639 under-predicted, but Nielsen (1992) notes that f_w and C_f are very similar for friction coefficients >0.05,
640 so by ignoring the phase lag between the flow velocity and bed sheer stress we could assume that $f_w =$
641 C_f at PTW, which would increase the empirically-derived C_f towards that derived from the model
642 calibration.

643 After optimisation of the numerical model, typical rms errors between predicted and observed H_s are
644 consistently small (3 – 10 cm) and the distribution of wave energy dissipation is generally well
645 replicated (Figure **16**). The model results indicate that breaking wave dissipation dominates across all
646 platforms except PTW and, in line with the field observations, do not show any systematic variations
647 in the wave height decay between sites that can be linked to platform roughness. The predicted $H_{s,inc}/h$
648 compare well with the observations at the majority of the platform sites, in particular DOL, LST and
649 PTW, which all display the strong landwards increase in $H_{s,inc}/h$ associated with the increasing
650 proportion of broken wave bores towards the shoreline. This suggests that the Rayleigh distribution
651 inherent in the model formulation (Eq. 5 and Figure 1) can be used to successfully parameterise the
652 wave height dissipation by wave breaking across the majority of the rock platforms studied.

653 The results of the numerical model generally agree well with the field observations (i.e., Figure **16**)
654 and the range of computed $H_{s,inc}/h$ fall within the expected range between sandy beaches and coral
655 reefs; however, there are concerns about the calibration of C_f that question the suitability of the model.
656 This is highlighted by the very high optimised C_f for PTW (0.34), the roughest platform, and the very
657 low optimised C_f for FWR (0.005), also a very rough site. In the present study, both C_f and γ are
658 independently calibrated, while in studies of wave propagation over reefs it is common to fix one of
659 the dissipation parameters and calibrate for the other (e.g., Lowe et al., 2005; Péquignet et al., 2011).
660 When the optimised C_f is replaced by Nielsen's (1992) empirical estimate (or the data-derived values)
661 and the model is recalibrated for γ, larger rms errors for $H_{s,inc}$ are obtained (not shown). Certainly, for
662 the roughest platforms PTW and FWR, the ratio A_b/k_w in **Eq. (17)** for the incident-wave frequencies
663 approaches unity, which means that the wave orbital length-scale is similar to the roughness length
664 scale (Madsen, 1994). This may imply that the numerical model used here incorrectly parameterises
665 the physics of wave-roughness interaction across a very rough rock platform, and suggests an
666 alternative parameterisation may be required. One approach could be to specify a relative roughness
667 linked to the large-scale morphology of individual platform roughness elements. These are often of a
668 similar height or diameter to the surf zone water depth and directly affect the passage of waves, which
669 must flow around and over such structures. A parameterisation similar to that of flow through
670 canopies, where $f_w \propto \alpha_w$, may be more appropriate, where α_w is the ratio of the flow in the canopy to

that just above the canopy, which is shown to depend on the ratio of the spacing of the canopy elements to A_b (e.g., Lowe et al., 2007; Huang et al., 2012; Monismith et al., 2015). Therefore, for very rough rock platforms, frictional drag may scale with the ratio of the rock element spacing to A_b; however, this requires further investigation by field observation and higher-order numerical modelling, since Rodgers et al. (2016) do correlate f_w to A_b/k_w across an exceptionally rough coral reef.

6.3 Implications for wave dissipation over rock platforms

Under the conditions during which we collected our data, there does not appear to be a significant impact of roughness on wave energy dissipation; however, there may be conditions when bed friction becomes important (e.g., Lowe et al., 2005). Whilst we have some concerns about the applicability of several of the model results, there is sufficient confidence, inspired by the good fit in Figure **16** and the skilful quantification of $H_{s,inc}/h$ across our middle range of sites, to use the model to investigate the importance of frictional dissipation across a shore platform.

Wave energy dissipation by bed friction ε_f was integrated across the intertidal region of a Type A shore platform for varying wave conditions, bed gradients and C_f values. Two of these parameters were fixed at the mean observed values and a number of simulations were run by varying the remaining input parameters (Figure **17**). The relative importance of frictional dissipation increases with decreasing wave height and bed gradient, and increasing bed roughness. The absolute values for the wave dissipation by friction increase with increasing wave height and bed roughness, and decreasing bed gradient. These results indicate that frictional dissipation is only significant on platforms that are very rough ($C_f > 0.1$), low-gradient ($\tan\beta < 0.02$) and/or subjected to small wave conditions ($H_o < 0.5$ m), where friction may account for ~20 % of the total wave energy dissipation. However, under small waves, the absolute amount of energy dissipated is very small (< 1 kW m^{-2}), so across these very rough flat platforms the total amount of frictional dissipation scales with H_o. This implies that over the majority of Type A rock shore platforms short-wave breaking is the dominant source of dissipation and the effects of bottom friction are small (<10 % of the total), so can probably be disregarded in wave energy balance models. Further analysis using models with more physical processes (e.g., phase-resolving, or surf-beat models) is required to similarly investigate the sensitivity of nearshore currents and infragravity waves to the bed roughness of the platforms.

Finally, we briefly revisit the morphological implications of our findings to discuss the role of wave action in the evolution of rocky coasts. Type A shore platforms primarily dissipate energy by wave breaking, which drives mean near-bed currents through the generation of radiation stress gradients (Longuet-Higgins and Stewart, 1962). These currents will impart a drag force onto the rock surface, acting to cause direct platform erosion (e.g., through hydraulic plucking of weathered, fractured rock), and abrasion by the transport of loose materials across its surface (Sunamura, 1992). Wave dissipation by bed friction is of secondary importance and it is only important where the turbulence associated with the broken waves reaches the bed at the shallow landward extreme of the platform that wave forces have a direct effect on platform erosion. This conjures up an image of a wide turbulent surf zone, effective at dissipating wave energy, but only able to leverage this energy for doing geomorphological work within a narrow shallow-water region. This narrow turbulent region, comprising of the swash and inner surf zone, migrates twice-daily across the platform due to the tide, and it is in this zone where most of the geomorphic work is considered being done. Considering platforms such as DOL with slab-like steps in the upper-profile, we may expect slabs to be loosened by direct wave forcing and then removed by the mean wave-generated near-bed currents (Stephenson and Naylor, 2011). Conversely, at HLQ wave-generated currents are probably focused into the channels formed by the cross-shore orientation of the bedding planes, directly eroding rock fragments

716 and causing abrasion. Lastly, it appears to be the gradient of the Type A platform that determines the
717 delivery of wave energy, and hence potential for cliff toe erosion (Naylor et al., 2010), by controlling
718 the cross-shore distribution of the rate of wave breaking dissipation. We thereby suggest that for the
719 purposes of determining the role of waves in cliff erosion and rocky shore evolution, the majority of
720 Type A shore platforms may be modelled in a similar manner to a sandy beach.

721 **7. Conclusions**

722 Here we present for the first time a comprehensive analysis of wave transformation across sloping
723 (Type A) rock shore platforms. Observations from five platforms, all with contrasting surface
724 roughness, gradient and wave climate, represent the most extensive ever collected on rock shore
725 platforms and demonstrate that frictional dissipation by platform roughness is of secondary
726 importance compared to wave breaking dissipation. This is similar to observations on smooth sandy
727 beaches, but is in contrast to rough coral reef platforms where friction has been observed to dominate.
728 Rock platforms are shown to dissipate both incident and infragravity wave energy and, in line with
729 previous studies, surf zone wave heights are saturated and strongly tidally-modulated. Waves develop
730 skewness and asymmetry across the platforms, and the relative wave height to water depth ratio scales
731 with platform gradient. Overall, comparisons between the observed properties of the waves and
732 formulations derived from sandy beaches has not highlighted any systematic variations between the
733 sites that can be attributed to (differences in) platform roughness.

734 Optimisation of a simple numerical wave transformation model provides further exploration of the
735 frictional and wave breaking parameter space. The breaker criterion falls between the range of values
736 reported for flat sandy beaches and steep coral fore-reefs, lending further support to the control by
737 platform gradient; however, the optimised drag coefficient for frictional wave dissipation is
738 significantly scattered for the roughest sites. Further exploration using an empirical drag coefficient
739 does not improve performance and suggests that high-order numerical wave models are required to
740 successfully parameterise frictional dissipation over the roughest platforms.. Model simulations using
741 a range of average data from our most typical platforms indicate that friction accounts for ~10 % of
742 the total intertidal short-wave dissipation under modal wave conditions, only becoming significant
743 (~20 %) across very rough, flat platforms, under small wave conditions. Overall, observational and
744 modelling results suggest that frictional dissipation of short-wave energy can probably be neglected
745 for the majority of Type A rock platforms, particularly inside the surf zone, which can be treated
746 similarly to sandy beaches when assessing wave energy delivery to the landward end of the platforms.

747 **Acknowledgements**

748 This research was funded by EPSRC grant EP/L02523X/1, Waves Across Shore Platforms, awarded
749 to GM and MJA. We would like to thank our field and technical team: Peter Ganderton, Tim Scott,
750 Olivier Burvingt, Pedro Almeida, Kris Inch and Kate Adams. The data on which this paper is based is
751 available from TP or via the online repository found at http://hdl.handle.net/10026.1/9105. The
752 authors would like to thank the reviewers who provided valuable feedback, insight and comment on
753 the original manuscript and, we believe, improved the work as a result.

754

755 **8. References;**

756 Battjes, J.A., and J.P. Janssen (1978). Energy loss and setup due to breaking of random waves. Proc.
757 16th ICCE, ASCE, 569-588, doi 10.1061/9780872621909.034.
758
759 Beetham, E., and P.S. Kench (2011). Field observations of infragravity waves and their behaviour on
760 rock shore platforms. ESPL, doi: 10.1002/esp.2208.

Brander, R. W., P. S. Kench, and D. Hart (2004), Spatial and temporal variations in wave characteristics across a reef platform, Warraber Island, Torres Strait, Australia, *Marine Geology*, *207*(1–4), 169-184.Doi: 10.1016/j.margeo.2004.03.014.

De Bakker, A.T.M., Brinkkemper, J.A., Van der Steen, Florian, Tissier, M.F.S. & Ruessink, B.G. (2016). Cross-shore sand transport by infragravity waves as a function of beach steepness. *Journal of geophysical research. Earth surface*, 121 (14 p.).

Dickson, M. E., M. J. A. Walkden, and J. W. Hall (2007), Systemic impacts of climate change on an eroding coastal region over the twenty-first century, *Climatic Change*, *84*(2), 141-166. Doi: 10.1007/s10584-006-9200-9.

Dickson, M. E., and R. Pentney (2012), Micro-seismic measurements of cliff motion under wave impact and implications for the development of near-horizontal shore platforms, *Geomorphology*, *151–152*, 27-38. Doi: 10.1016/j.geomorph.2012.01.006.

Dickson, M. E., H. Ogawa, P. S. Kench, and A. Hutchinson (2013), Sea-cliff retreat and shore platform widening: steady-state equilibrium?, *Earth surface processes and landforms*, *38*(9), 1046-1048. Doi: 10.1002/esp.3422.

Doering, J. C., and A. J. Bowen (1995), Parametrization of orbital velocity asymmetries of shoaling and breaking waves using bispectral analysis, *Coastal Engineering*, *26*(1-2), 15-33. Doi: 10.1016/0378-3839(95)00007-X.

Farrell, E. J., H. Granja, L. Cappietti, J. T. Ellis, B. Li, and D. J. Sherman (2009), Wave Transformation across a Rock Platform, Belinho, Portugal, *Journal of Coastal Research*, 44-48.

Falter, J. L., M. J. Atkinson, M. A. Merrifield (2004), Mass-transfer of nutrient uptake by a wave-dominated reef flat community, *Limnology and Oceanography*, 49(5), 1820-1831.

Hardy, T. A., and I. R. Young (1996), Field study of wave attenuation on an offshore coral reef, *Journal of Geophysical Research: Oceans*, *101*(C6), 14311-14326.Doi: 10.1029/96JC00202

Huang, Z.-C., L. Lenain, W. K. Melville, J. H. Middleton, B. Reineman, N. Statom, and R. M. McCabe (2012), Dissipation of wave energy and turbulence in a shallow coral reef lagoon, *Journal of Geophysical Research: Oceans*, *117*(C3). Doi: 10.1029/2011JC007202

Inch, K., Davidson, M., Masselink, G. and Russell, P., (2017), Observations of nearshore infragravity wave dynamics under high energy swell and wind-wave conditions. *Continental Shelf Research*, *138*, 19-31.

Kench, P. S., R. W. Brander, K. E. Parnell, and R. F. McLean (2006), Wave energy gradients across a Maldivian atoll: Implications for island geomorphology, *Geomorphology*, *81*(1–2), 1-17.

Kennedy, D. M., and J. Milkins (2015), The formation of beaches on shore platforms in microtidal environments, *Earth surface processes and landforms*, *40*(1), 34-46. Doi: 10.1002/esp.3610

Kennedy, D. M., R. Paulik, and M. E. Dickson (2011), Subaerial weathering versus wave processes in shore platform development: reappraising the Old Hat Island evidence, *Earth surface processes and landforms*, *36*(5), 686-694. Doi: 10.1002/esp.2092

Kobayashi, N., and A. Wurjanto (1992), Irregular Wave Setup and Run-up on Beaches, *Journal of Waterway, Port, Coastal, and Ocean Engineering*, *118*(4), 368-386.Doi: 10.1061/(ASCE)0733-950X(1992)118:4(368)

Komar, P.D., 1998. Beach Processes and Sedimentation. Prentice-Hall, Upper Saddle River, NJ, 544 pp.

Lowe, R. J., J. L. Falter, M. D. Bandet, G. Pawlak, M. J. Atkinson, S. G. Monismith, and J. R. Koseff (2005), Spectral wave dissipation over a barrier reef, *Journal of Geophysical Research: Oceans*, *110*(C4). Doi: 10.1029/2004JC002711.

Lowe, R. J., J. L. Falter, J. R. Koseff, S. G. Monismith, and M. J. Atkinson (2007), Spectral wave flow attenuation within submerged canopies: Implications for wave energy dissipation, *Journal of Geophysical Research: Oceans*, *112*(C5), 1 – 14. Doi: 10.1029/2006JC003605

Madsen, O. S., 1994. Spectral wave-current bottom boundary layer flows, in Coastal Engineering 1994: Proceedings of the Twenty-Fourth International Conference, edited by B. L. Edge, pp. 623 – 634, Am. Soc. of Civ. Eng., Reston, Va.

Marshall, R. J. E., and W. J. Stephenson (2011), The morphodynamics of shore platforms in a micro-tidal setting: Interactions between waves and morphology, *Marine Geology*, *288*(1–4), 18-31.Doi: 10.1016/j.margeo.2011.06.007

May, V.J. and Hansom, J.D., (2003). Coastal Geomorphology of Great Britain, Geological Conservation Review Series, No. 28, Joint Nature Conservation Committee, Peterborough, 754 pp.

Masselink, G. and Hegge, B., (1995). Morphodynamics of meso- and macrotidal beaches: examples from central Queensland, Australia. *Marine Geology*, 129(1-2): 1-23.Doi: 10.1016/0025-3227(95)00104-2

McCall, R., Masselink, G., Austin, M., Poate, T. and Jager, T., (2017) Modelling Incident-Band and infragravity wave dynamics on rocky shore platforms. Proceedings of Coastal Dynamics 2017, Denmark. Pp1658-1669.

Monismith, S. G., J. S. Rogers, D. Koweek, and R. B. Dunbar (2015), Frictional wave dissipation on a remarkably rough reef, *Geophysical Research Letters*, *42*(10), 4063-4071.
Doi: 10.1002/2015GL063804.

Naylor, L. A., W. J. Stephenson, and A. S. Trenhaile (2010), Rock coast geomorphology: Recent advances and future research directions, *Geomorphology*, *114*(1–2), 3-11.Doi: 10.1016/j.geomorph.2009.02.004.

Nielsen, P., (1992). Coastal bottom boundary layers and sediment transport. Advanced Series on Ocean Eng. vol. 4. World Scientific, Singapore, pp. 324.

Nielsen, P., (1989). Analysis of Natural Waves by Local Approximations. *Journal of Waterway, Port, Coastal, and Ocean Engineering*, 115(3): 384-396.Doi: 10.1061/(ASCE)0733-950X(1989)115:3(384).

Nelson RC. (1994). Depth limited design wave heights in very flat regions. *Coastal Engineering* 23(1 – 2): 43 – 59.Doi: 10.1016/0378-3839(94)90014-0.

Nott, J. (2003), Waves, coastal boulder deposits and the importance of the pre-transport setting, *Earth and Planetary Science Letters*, *210*(1–2), 269-276.
Doi: 10.1016/S0012-821X(03)00104-3.

867 Ogawa, H., Dickson, M. E., & Kench, P. S. (2015). Hydrodynamic constraints and storm wave
868 characteristics on a sub-horizontal shore platform. *Earth Surface Processes and Landforms*, 40(1), 65-
869 77. Doi:10.1002/esp.3619.
870
871 Ogawa, H., M. E. Dickson, and P. S. Kench (2016), Generalised observations of wave characteristics
872 on near-horizontal shore platforms: Synthesis of six case studies from the North Island, New Zealand,
873 *New Zealand Geographer*, *72*(2), 107-121. Doi: 10.1111/nzg.12121.
874
875 Ogawa, H., M. E. Dickson, and P. S. Kench (2011), Wave transformation on a sub-horizontal shore
876 platform, Tatapouri, North Island, New Zealand, *Continental Shelf Research*, *31*(14), 1409-1419.
877 Doi:10.1016/j.csr.2011.05.006
878
879 Ogawa, H., M.E. Dickson, P.S. Kench, (2012). Field measurements of wave characteristics on a near-
880 horizontal shore platform, Oraka, NZ. *Geographical Research.,* 50, 179-192.
881
882 Pethick, J., (1984). An introduction to coastal Geomorphology. Edward Arnold, London
883
884 Poate, T.G.; G. Masselink, M. Austin, M.E. Dickson, and P. Kench, (2016). Observations of Wave
885 Transformation on Macro-Tidal Rocky Platforms. In: Vila-Concejo, A.; Bruce, E.; Kennedy, D.M.,
886 and McCarroll, R.J. (eds.), Proceedings of the 14th International Coastal Symposium (Sydney,
887 Australia). Journal of Coastal Research, Special Issue, No. 75, pp. 602-606. Coconut Creek (Florida),
888 ISSN 0749-0208.
889
890 Raubenheimer, B., R. T. Guza, and S. Elgar (1996), Wave transformation across the inner surf zone,
891 *Journal of Geophysical Research: Oceans*, *101*(C11), 25589-25597. Doi: 10.1029/96JC02433.
892
893 Rogers, J. S., S. G. Monismith, D. A. Koweek, and R. B. Dunbar (2016), Wave dynamics of a Pacific
894 Atoll with high frictional effects, *Journal of Geophysical Research: Oceans*, *121*(1), 350-
895 367.Ruessink, B. G., G. Ramaekers, and L. C. van Rijn (2012), On the parameterization of the free-
896 stream non-linear wave orbital motion in nearshore morphodynamic models, *Coastal Engineering*, *65*,
897 56-63.Doi: 10.1016/j.coastaleng.2012.03.006
898
899 Sallenger, A. H., and R. A. Holman (1985), Wave energy saturation on a natural beach of variable
900 slope, *Journal of Geophysical Research: Oceans*, *90*(C6), 11939-11944.
901 Doi: 10.1029/JC090iC06p11939.
902
903 Stephenson, W. J., and L. A. Naylor (2011), Geological controls on boulder production in a rock
904 coast setting: Insights from South Wales, UK, *Marine Geology*, *283*(1–4), 12-24.Doi:
905 10.1016/j.margeo.2010.07.001.
906
907 Stephenson, W. J., and R. M. Kirk (2000), Development of shore platforms on Kaikoura Peninsula,
908 South Island, New Zealand: Part One: The role of waves, *Geomorphology*, *32*(1–2), 21-41.Doi:
909 10.1016/S0169-555X(99)00061-6.
910
911 Sunamura, T., 1992. Geomoprhology of Rocky Coasts, Wiley and Sons, New York. 302pp
912 Thornton, E. B., and R. T. Guza (1983), Transformation of wave height distribution, *Journal of*
913 *Geophysical Research: Oceans*, *88*(C10), 5925-5938. Doi: 10.1029/JC088iC10p05925.
914
915 Symonds, G., K. P. Black, and I. R. Young (1995), Wave-driven flow over shallow reefs, *Journal of*
916 *Geophysical Research: Oceans*, *100*(C2), 2639-2648. Doi: 10.1029/94JC02736.
917
918 Trenhaile, A. S. (1987), *The geomorphology of rock coasts*, Oxford University Press, Incorporated,
919 384 p.
920

Trenhaile, A.S., (1999). The width of shore platforms in Britain, Canada, and Japan. *Journal of Coastal Research,*15, 355 – 364.

Trenhaile, A. S., and J. I. Kanyaya (2007), The Role of Wave Erosion on Sloping and Horizontal Shore Platforms in Macro- and Mesotidal Environments, *Journal of Coastal Research*, 298-309.Doi: 10.2112/04-0282.1.

Thornton, E. B., and R. T. Guza (1982), Energy saturation and phase speeds measured on a natural beach, *Journal of Geophysical Research: Oceans*, *87*(C12), 9499-9508. Doi: 10.1029/JC087iC12p09499.

van Gent, M.R.A., 2001. (2001), Wave Runup on Dikes with Shallow Foreshores, *Journal of Waterway, Port, Coastal, and Ocean Engineering*, *127*(5).Doi: 10.1061/(ASCE)0733-950X(2001)127:5(254).

Vetter, O., J. M. Becker, M. A. Merrifield, A. C. Pequignet, J. Aucan, S. J. Boc, and C. E. Pollock (2010), Wave setup over a Pacific Island fringing reef, *Journal of Geophysical Research: Oceans*, *115*(C12), 1-13. Doi: 10.1029/2010JC006455

Welch, P., (1967). The use of fast Fourier transform for the estimation of power spectra: a method based on time averaging over short, modified periodograms. *IEEE Transactions on Audio and Electroacoustics* 15 (2), 70 – 73.

Wright, L. D., P. Nielsen, A. D. Short, and M. O. Green (1982), Morphodynamics of a macrotidal beach, *Marine Geology*, *50*(1-2), 97-127.

Table 1 – Summary data for each deployment site; PT = Pressure sensor, ODN = Ordnance datum Newlyn, tanβ = slope along PT array, H_s = significant wave height, T_p = peak wave height, H_b = breaker wave height, h_b = breaker water depth.

Parameters		**Sites**					
		DOL	**FWR**	**FWB**	**LST**	**HLQ**	**PTW**
Deployment Data	Duration (tides)	13	8	8	8	12	8
	# PTs	15	14	5	15	12	12
	# Vectors	2	2	0	2	2	2
	PT spacing (m)	~10	~10	~15	~15	~10	~15
	PT z range m ODN (min, max)	-1.77, 1.66	-0.67, 2.12	-1.64, -0.95	-1.46, 3.14	-1.82, 0.46	-1.9, 2.35
	PT x range (m)	100	150	60	225	115	170
	Video (hrs)	32	36	36	11	38	19
Platform Morphology	Intertidal platform width (m)	160	210	210	325	140	180
	Bedrock	Limestone	Sandstone	n/a	Mudstone	Sandstone/ shale	Slate/siltstone
	Average tanβ between PT s	0.031	0.018	0.011	0.021	0.030	0.028
	Roughness (alongshore average, k_σ / k_R)	0.072/0.020	0.144/0.062	0.008/0.002	0.068/0.015	0.104/0.029	0.172/0.090
	Mean spring tide range (mODN), mean low water spring (mODN)	4.2, 0.2	6.4, -3.1	6.4, -3.1	10.7, -5	7.3, -4.1	4.5, -2.1
Hydrodynamics	H_s (min, max)	0.30, 1.87	0.52, 2.69	0.35, 3.03	0.11, 1.75	0.65, 1.60	0.42, 1.71
	T_p (min, max)	8.94, 17	8.37, 16	8.2, 15.5	5.8, 9.4	7.5, 10.1	7.3, 13.9

	H_b (min, max)	0.73, 1.65	1.66, 2.37	1.83, 2.46	0.55, 1.56	1.08, 1.56	0.72, 1.04
	h_b (min, max)	1.73, 3.36	3.49, 4.04	4.30, 5.09	2.19, 3.52	3.52, 4.35	4.17, 4.48
	H^2T_p (min, max)	5.1, 43.8	28.4, 107.2	33.0, 134.4	6.8, 22.8	9.7, 18.41	4.0, 22.3

Table 2 – Summary of platform gradient ($\tan\beta$), roughness length-scale (k_σ) and empirical drag coefficient ($C_{f,Nielsen}$; **Eq. 17**), and numerical model short-wave dissipation parameters, averaged over four tidal cycles for all field sites. Model parameters are: optimised drag coefficient (C_f), rms and significant breaker criterion (γ), ratio of frictional to breaker dissipation ($\langle \varepsilon_f / \varepsilon_b \rangle$), and wave height to water depth ratio ($H_{s,inc}/h$).

	Observed			**Computed**				
	$\tan\beta$	k_σ	$C_{f,Nielsen}$	C_f	γ_{rms}	γ_s	$\langle \varepsilon_f / \varepsilon_b \rangle$	$H_{s,inc}/h$
DOL	0.031	0.072	0.0367	0.0502	0.36	0.51	0.142	0.69
FWR	0.018	0.144	0.0388	0.0005	0.53	0.71	0.002	0.68
LST	0.021	0.068	0.0225	0.0005	0.60	0.84	0.002	0.68
HLQ	0.03	0.104	0.0336	0.049	0.44	0.62	0.140	0.61
PTW	0.028	0.172	0.0690	0.3413	0.66	0.93	3.820	0.54

Figure 1 – Effect of varying γ and C_f for wave transformation over a plane-sloping bed with $\tan\beta$ = 0.02 according to Thornton and Guza (1982) model. (a) Seabed gradient (solid line) and still water-level (dashed line). (b – d) H_s, ε_b and H_s/h for values of γ varied through the range indicated in the colorbar with C_f = 0.01. (e – g) H_s, ε_f and H_s/h for values of C_f shown in the colourbar and γ = 0.42.

Figure 2 – Location maps and aerial images of the five field sites; (a) Doolin (DOL), (b) Freshwater West (FWR & FWB), (c) Lilstock (LST), (d) Hartland Quay (HLQ) and (e) Portwrinkle (PTW).

Figure 3 – Cross-shore profiles for each of the field sites with locations of pressure transducers (black dots). The vertical bar in each of the panels represents the mean spring tidal range.

Figure 4 – Example identification of shoaling wave and surf zone conditions at Hartland Quay. (a) Rectified and merged video images across the shore platform with sensor locations (red dots) overlaid to identify regions of breaking (white) and shoaling waves (grey). (b) All data with water depth (h) plotted versus significant wave height (H_s) with blue and yellow symbols representing surf zone and shoaling waves, respectively. Red symbols represent the wave conditions coincident in (a). (c) Spatial and temporal variability in H_s for a single tidal cycle, with color scale running from 0.2 m (dark blue) to 1.4 m (yellow). Dashed line represent demarcation of the surf zone and the video image in (a) corresponds to the time 15:50 hrs (solid line).

Figure 5 – De-trended digital elevation models (DEMs) with PT locations (black circles) for all study sites with colour scale running from -1 (dark blue) and +1 m (yellow). Offshore is at the top of the DEMs. The two lines to the right of the DEMs represent the cross-shore variation in the alongshore-averaged roughness based on standard deviation k_σ and rugosity k_R.

Figure 6 – Time series of the significant wave height (H_s; solid line) and wave period (T_{spec}; dashed line) for each of the sites recorded by the nearest offshore wave buoy. Symbols (black circles) represent the tide-averaged significant breaker height for each of the monitored tides estimated from the pressure sensors deployed across the shore platforms.

Figure 7 – Left panels show incident significant wave height (H_s) versus normalised surf zone position (h/h_b) for all data runs with colour of the symbols representing the breaker height (H_b), with the colour bar running from 0.5 m (blue) to 3 m (yellow). Right panels show boxplots of relative wave height ($H_{s,inc}/h$) versus normalised surf zone position (h/h_b). On each box, the central mark (red line) is the median, the edges of the box are the 25th and 75th percentiles, the whiskers extend to the most

986 extreme data points not considered outliers (< 0.4th percentile or > 99.6th percentile).The dashed line
987 indicates the edge of the surfzone.

988 Figure 8 – Observed average (solid circles) and standard deviation (vertical bars) of H_{sinc}/h versus
989 normalised platform/beach slope ($\tan\beta/kh$) for all runs broken down for the different shore platform
990 sites. The data are binned corresponding to ± 0.025. The dashed line represents the prediction
991 according to Raubenheimer et al. (1996) represented by **Eq. (1)**.

992 Figure 9 – Boxplots of wave skewness (A_{skew}; left panels) and wave asymmetry (A_{asym}; right panels)
993 versus normalised surf zone position (h/h_b). On each box, the central mark (red line) is the median, the
994 edges of the box are the 25th and 75th percentiles, the whiskers extend to the most extreme data
995 points not considered outliers (< 0.4th percentile or > 99.6th percentile).

996 Figure 10 – Wave skewness(A_{skew}) and asymmetry (A_{asym}) as a function of the Ursell number (Ur)
997 derived from H_s. The gray dots are the individual estimates, the filled circles are the class mean values
998 based on binning the estimates according to $log(Ur)$ ±0.05. The vertical lines represent class standard
999 deviation for each bin. The dashed line shows the fits proposed by Ruessink et al. (2012).

1000 Figure 11 – Left panels show significant infragravity wave height ($H_{s,inf}$) versus normalised surf zone
1001 position (h/h_b) for all data runs with colour of the symbols representing the breaker height (H_b), with
1002 the colour bar running from 0.5 m (blue) to 3 m (yellow). Right panels show boxplots of percentage
1003 of infragravity energy ($\%Ig$) versus normalised surf zone position (h/h_b). On each box, the central
1004 mark (red line) is the median, the edges of the box are the 25th and 75th percentiles, the whiskers
1005 extend to the most extreme data points not considered outliers (< 0.4th percentile or > 99.6th
1006 percentile).

1007 Figure 12 – Scatter plot between the significant total infragravity wave height (H_{inf}) near the shoreline
1008 as a function of an incident wave power factor ($H_o^2T_p$). Each data point is a tide-averaged value where
1009 $0< h/hb <0.33$. The dashed line represents $H_{inf} = 0.004\ H_o^2T_p + 0.20$ from Inch et al. (2016).

1010 Figure 13 – Summary statistics for each site (all valid tides); (a) $H_{s,inc}/h$, (b) percentage infragravity
1011 energy (%Ig), (c) wave skewness (A_{skew}) and (d) wave asymmetry (A_{asym}). Circles are mean values
1012 and vertical bars represent the 95 % confidence interval ($= t(df) \times \sigma/\sqrt{n}$, where t is the t-statistic
1013 for the relevant degrees of freedom df and n is the number of observations).

1014 Figure 14 – Results of model calibration for C_f, with (left) ϵ_{abs} and (right) ϵ_{bias}. Black lines plot the
1015 mean error distribution over C_f -space over the four calibration tidal cycles with the shaded regions
1016 indicating the range. The black triangle is the tide-mean optimised C_f with 1 standard deviation
1017 plotted as the black horizontal error bar. The black dots indicate the final optimised C_f value for each
1018 field site. The grey horizontal line in the right-hand panels indicates zero bias.

1019 Figure 15 – Results of model calibration for γ, with (left) ϵ_{abs} and (right) ϵ_{bias}. Black lines plot the
1020 mean error distribution over γ-space over the four calibration tidal cycles with the shaded regions
1021 indicating the range. The black triangle is the tide-mean optimised γ with 1 standard deviation plotted
1022 as the black horizontal error bar. The black dots indicate the final optimised γ value for each field site.
1023 The grey horizontal line in the right-hand panels indicates zero bias.

1024 Figure 16 – Example model runs for each field site (lines) compared to field observations (triangles).
1025 (Bottom) Measured and modelled H_s indicating rms error. (Centre) Total wave energy dissipation,
1026 with predicted dissipation partitioned into ε_b (dash-dot line) and ε_f (red dashed line). (Top) Relative
1027 wave height H_s/h, indicating the model γ value (dotted line). Note different x-axis scales.

1028 Figure 17 – The behaviour of ε_f as a function of (a) H_o, (b) $\tan\beta$ and (c) C_f. Black curves (left axes)
1029 plot the % ε_f and red curves (right axes) plot the sum total ε_f across the inter-tidal region. γ was fixed
1030 at 0.5.

1031

1032

1033

Figure 1.

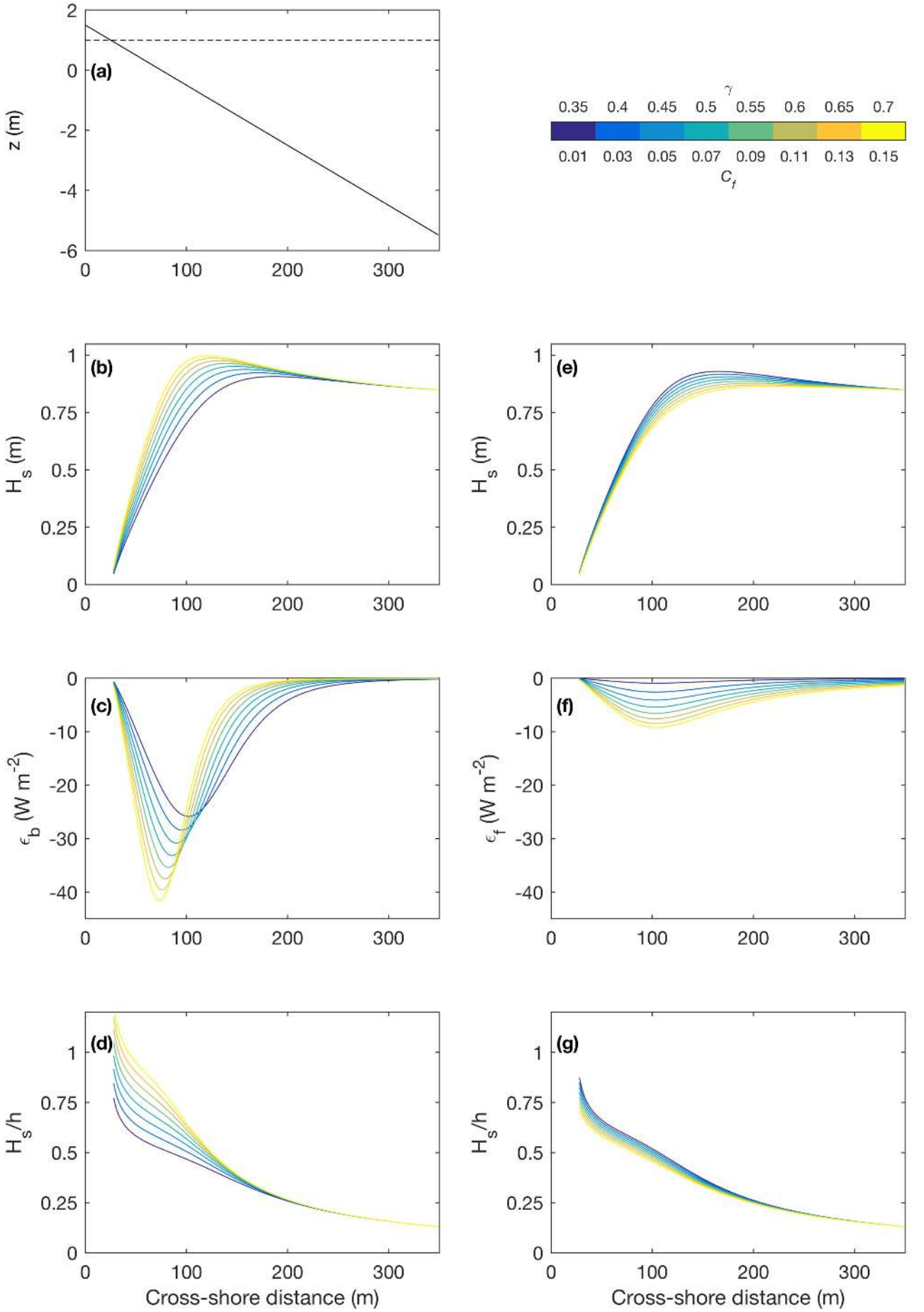
(a)
z (m)
2
0
-2
-4
-6
0
100
200
300
γ
0.35 0.4 0.45 0.5 0.55 0.6 0.65 0.7
0.01 0.03 0.05 0.07 0.09 0.11 0.13 0.15
C_f
(b)
(e)
H_s (m)
1
0.75
0.5
0.25
0
(c)
(f)
ϵ_b (W m^{-2})
ϵ_f (W m^{-2})
-10
-20
-30
-40
(d)
(g)
H_s/h
Cross-shore distance (m)

Figure 2.


(a) DOL
500m


(b) FWR, FWB


(c) LST
200m


(d) HLQ
100m


N
a
b
c
d
e

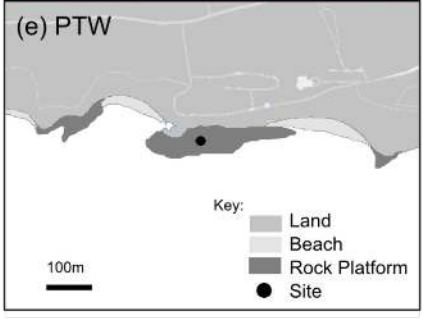
(e) PTW
Key:
Land
Beach
Rock Platform
Site
100m

Figure 3.

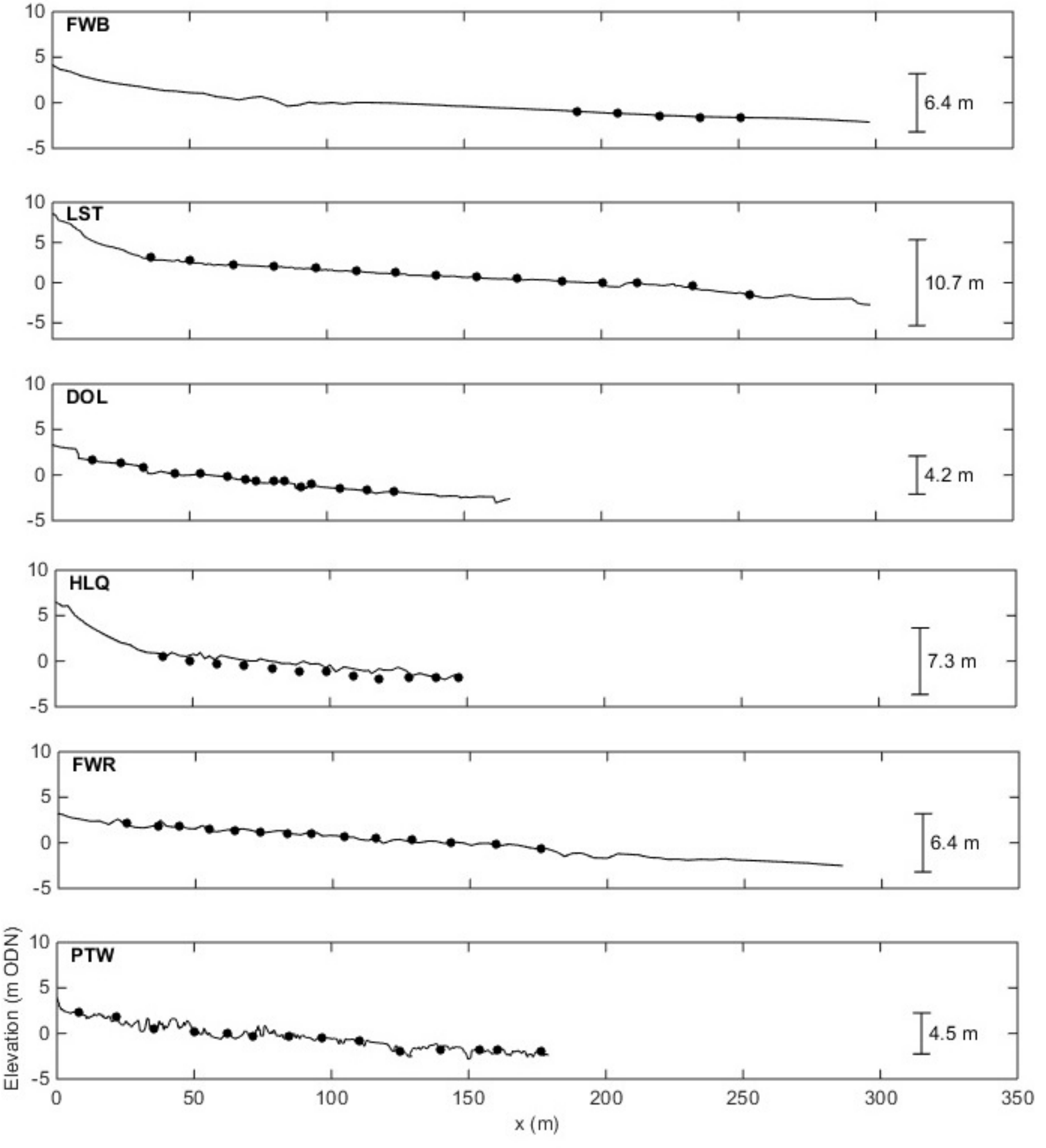
FWB
6.4 m
LST
10.7 m
DOL
4.2 m
HLQ
7.3 m
FWR
6.4 m
PTW
4.5 m
10
5
0
-5
Elevation (m ODN)
0
50
100
150
200
250
300
350
x (m)

Figure 4.

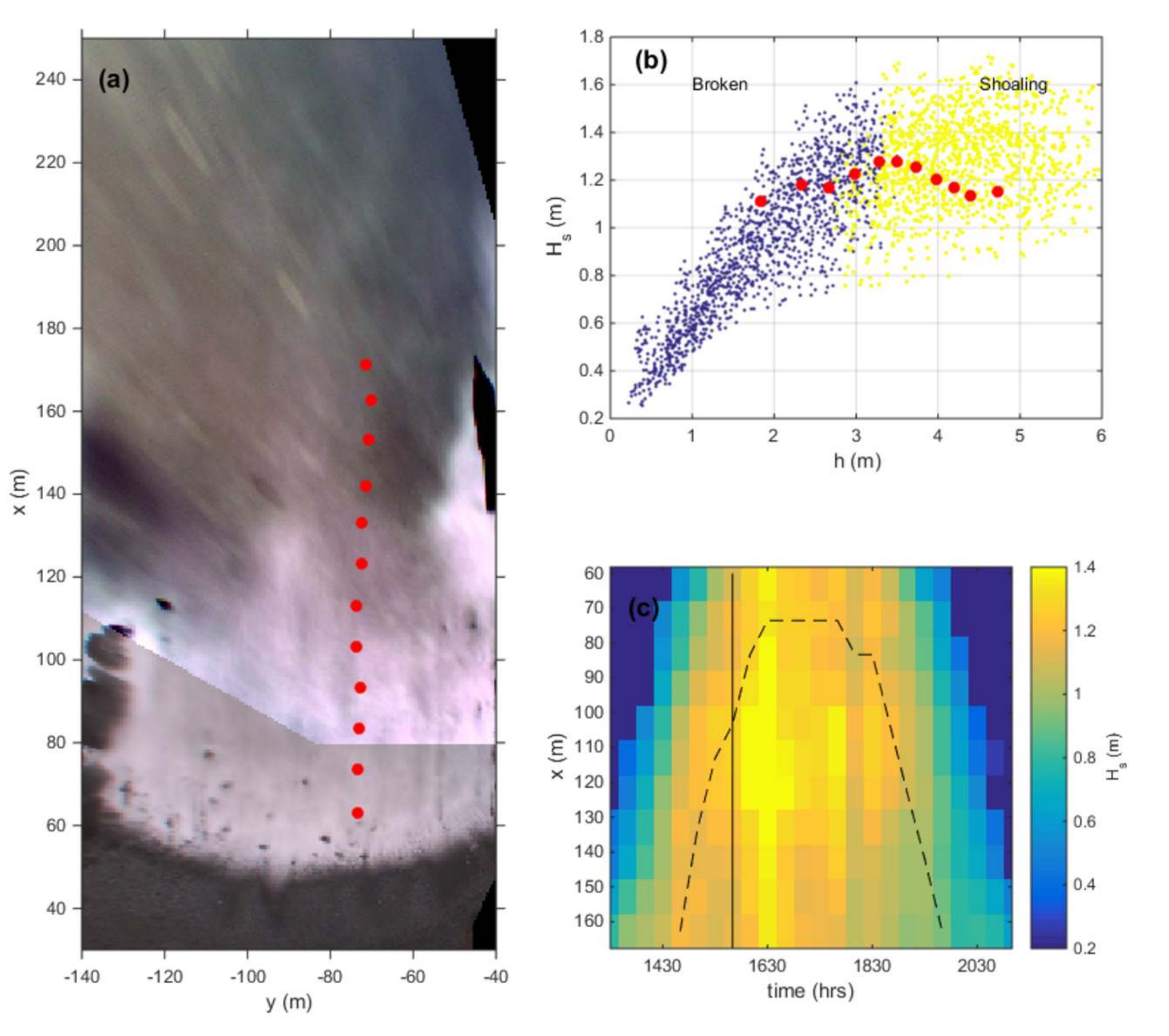
(a)
x (m)
y (m)
240
220
200
180
160
140
120
100
80
60
40
-140
-120
-100
-80
-60
-40
(b)
Broken
Shoaling
H_s (m)
h (m)
1.8
1.6
1.4
1.2
1
0.8
0.6
0.4
0.2
0
1
2
3
4
5
6
(c)
x (m)
time (hrs)
H_s (m)
60
70
80
90
100
110
120
130
140
150
160
1430
1630
1830
2030
1.4
1.2
1
0.8
0.6
0.4
0.2

Figure 5.

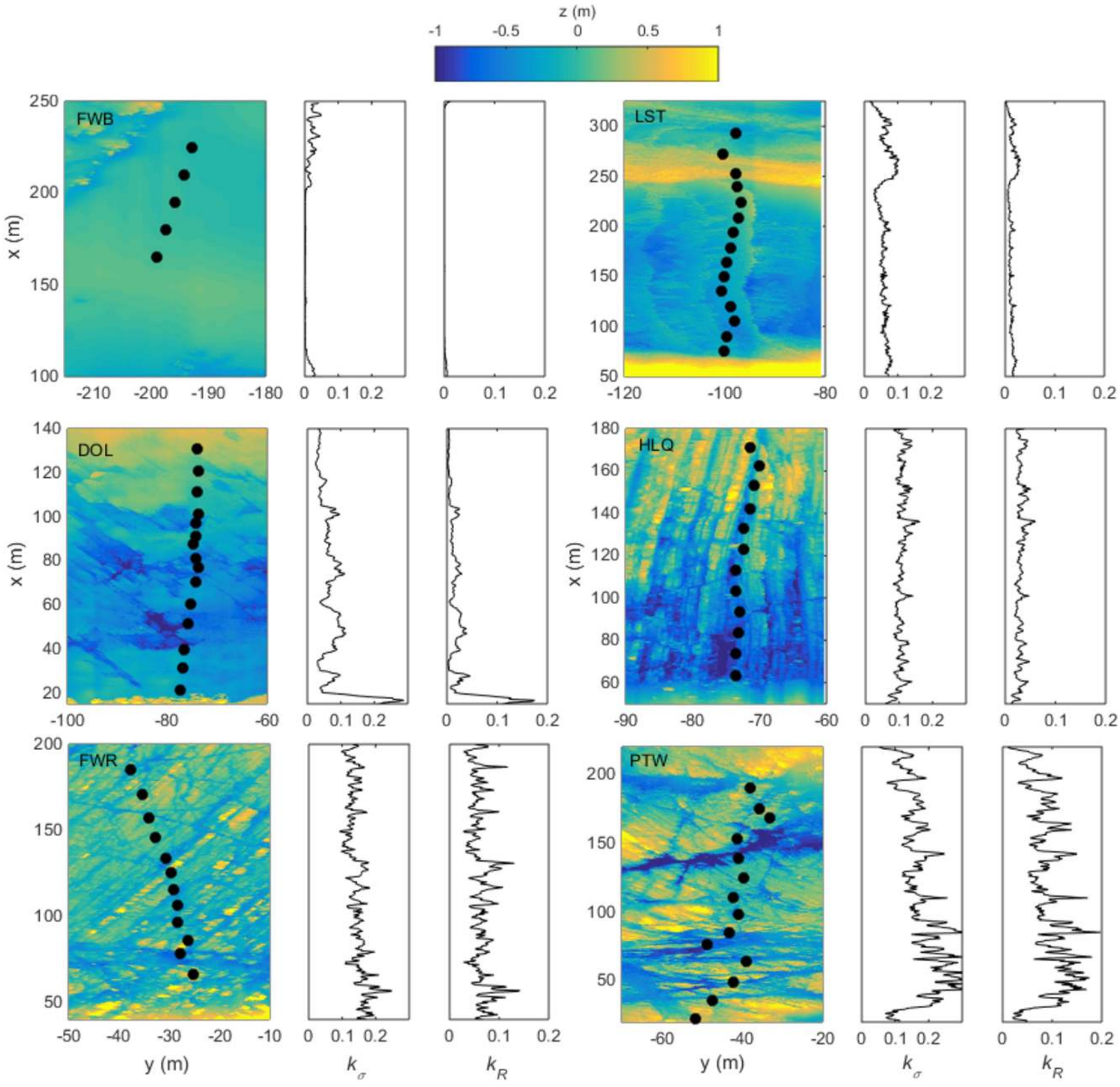
z (m)
-1
-0.5
0
0.5
1
FWB
LST
DOL
HLQ
FWR
PTW
x (m)
y (m)
k_σ
k_R

Figure 6.

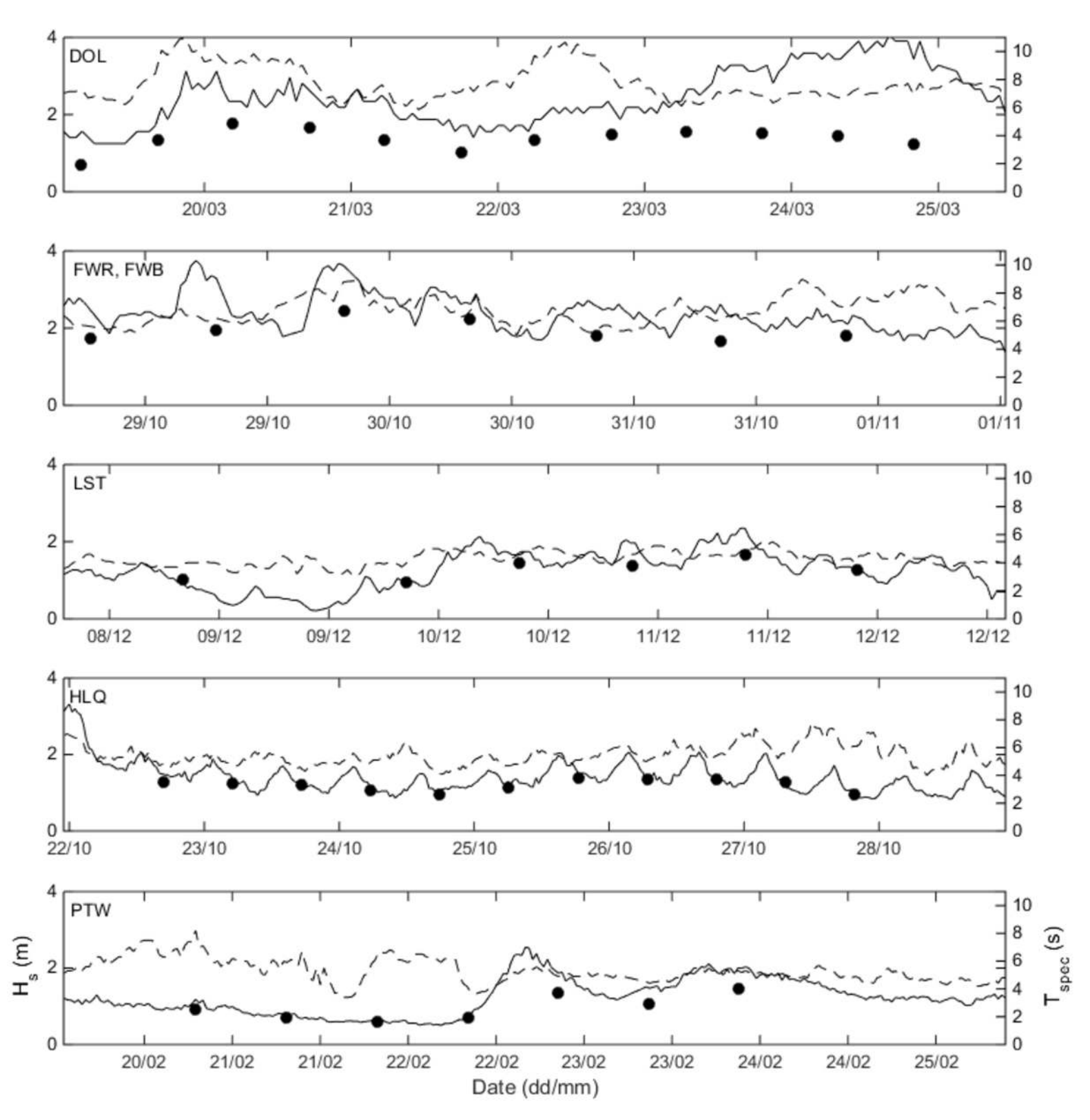
DOL
20/03
21/03
22/03
23/03
24/03
25/03
FWR, FWB
29/10
29/10
30/10
30/10
31/10
31/10
01/11
01/11
LST
08/12
09/12
09/12
10/12
10/12
11/12
11/12
12/12
12/12
HLQ
22/10
23/10
24/10
25/10
26/10
27/10
28/10
PTW
20/02
21/02
21/02
22/02
22/02
23/02
23/02
24/02
24/02
25/02
Date (dd/mm)
H_s (m)
T_{spec} (s)

Figure 7.

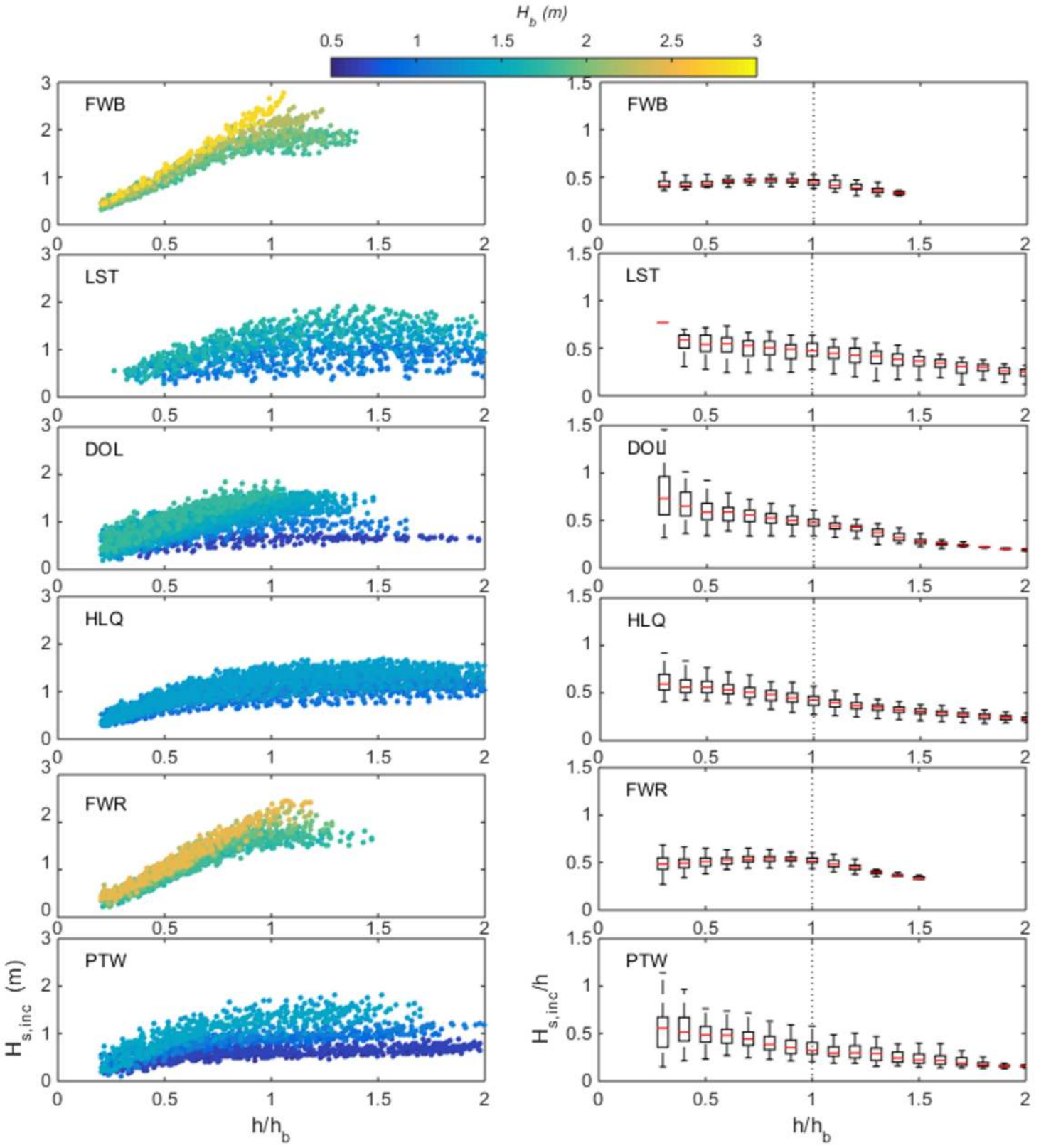
H_b (m)
0.5
1
1.5
2
2.5
3
FWB
LST
DOL
HLQ
FWR
PTW
$H_{s,inc}$ (m)
$H_{s,inc}/h$
h/h_b
h/h_b

Figure 8.

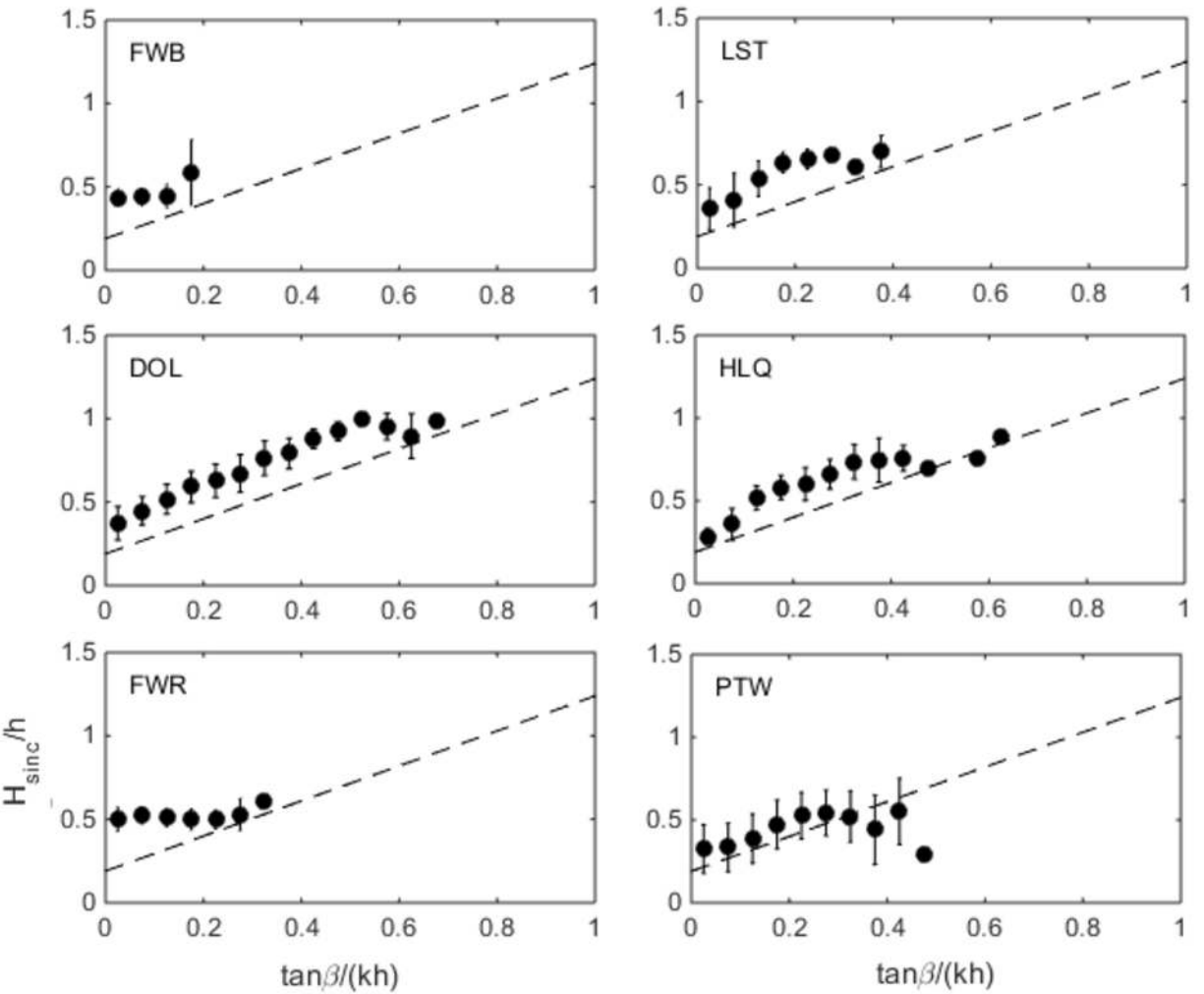
FWB
LST
DOL
HLQ
FWR
PTW
H_{sinc}/h
tanβ/(kh)
tanβ/(kh)

Figure 9.

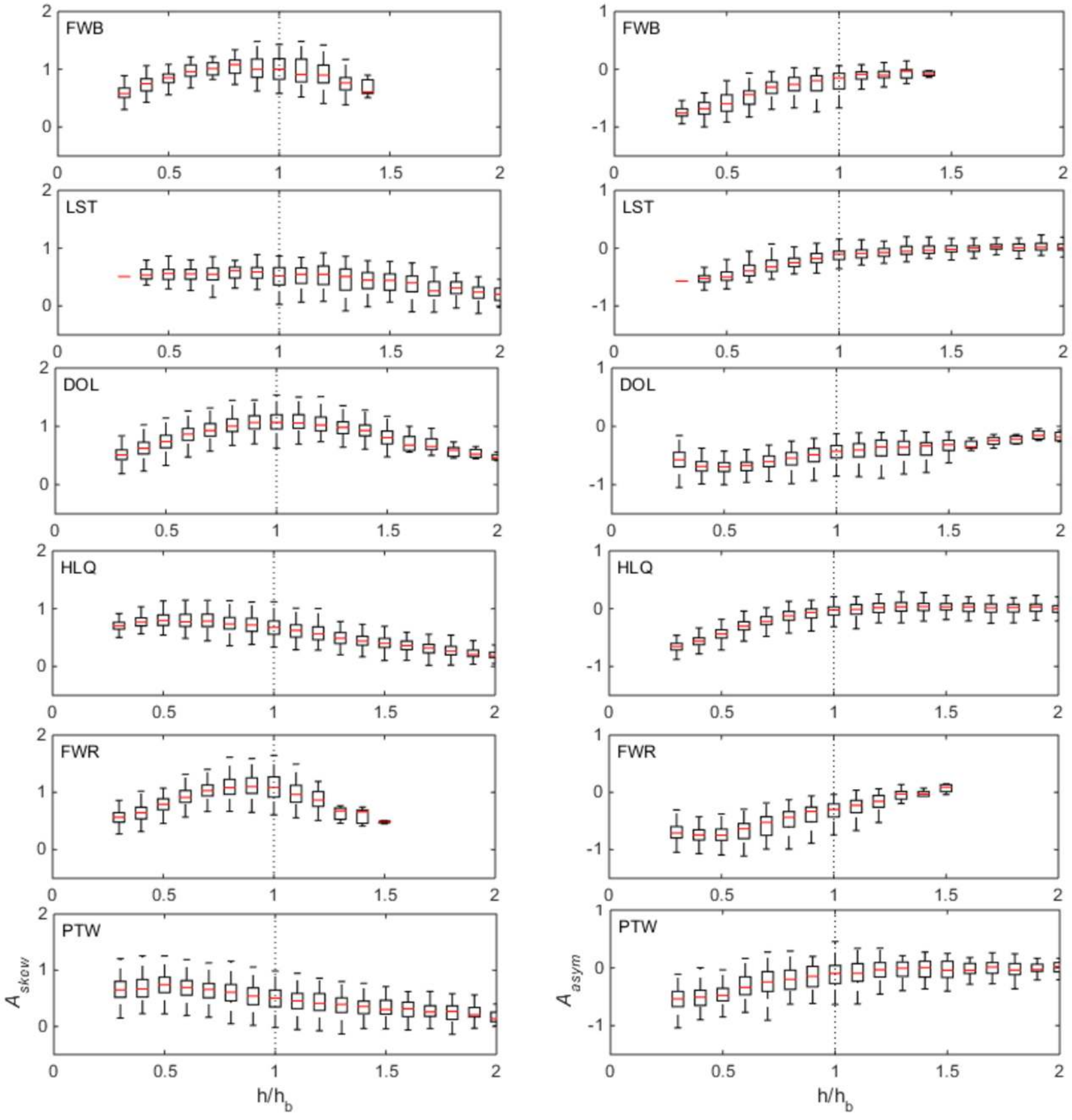
FWB
LST
DOL
HLQ
FWR
PTW
A_{skew}
A_{asym}
h/h$_b$
h/h$_b$

Figure 10.

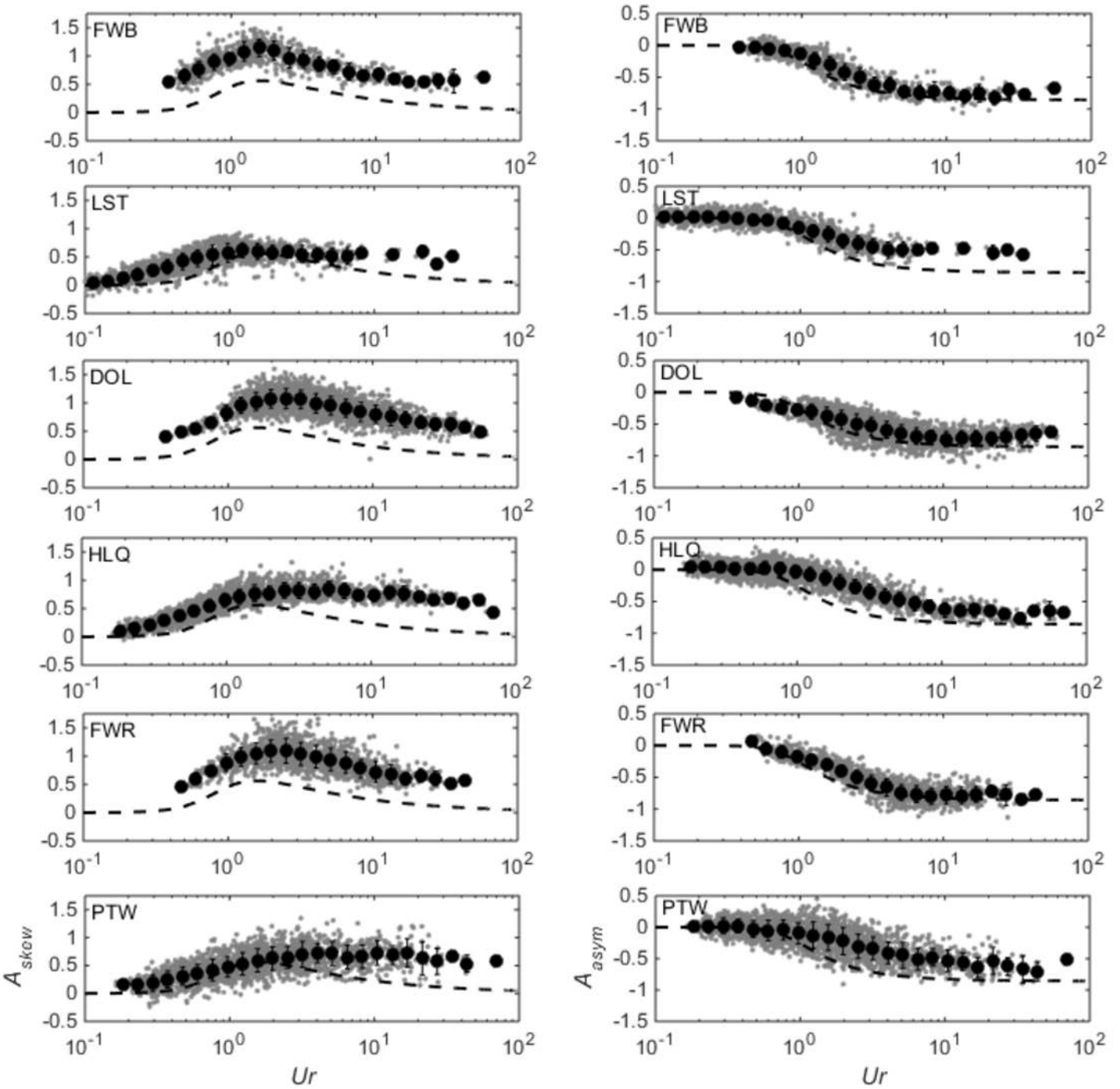
FWB
LST
DOL
HLQ
FWR
PTW
A_{skew}
A_{asym}
Ur
Ur

Figure 11.

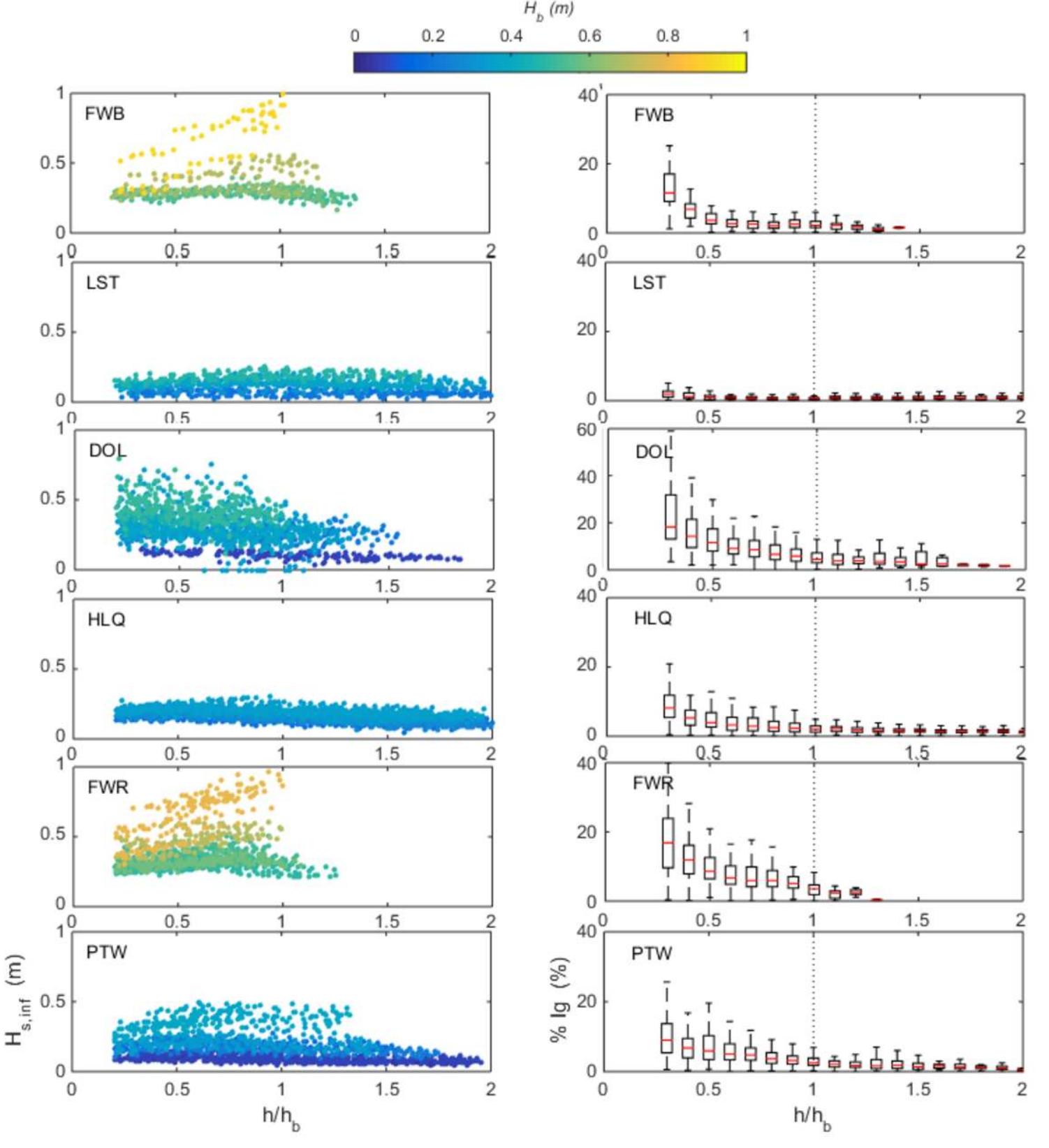
H_b (m)
0
0.2
0.4
0.6
0.8
1
FWB
LST
DOL
HLQ
FWR
PTW
$H_{s,inf}$ (m)
% Ig (%)
h/h_b
h/h_b

Figure 12.

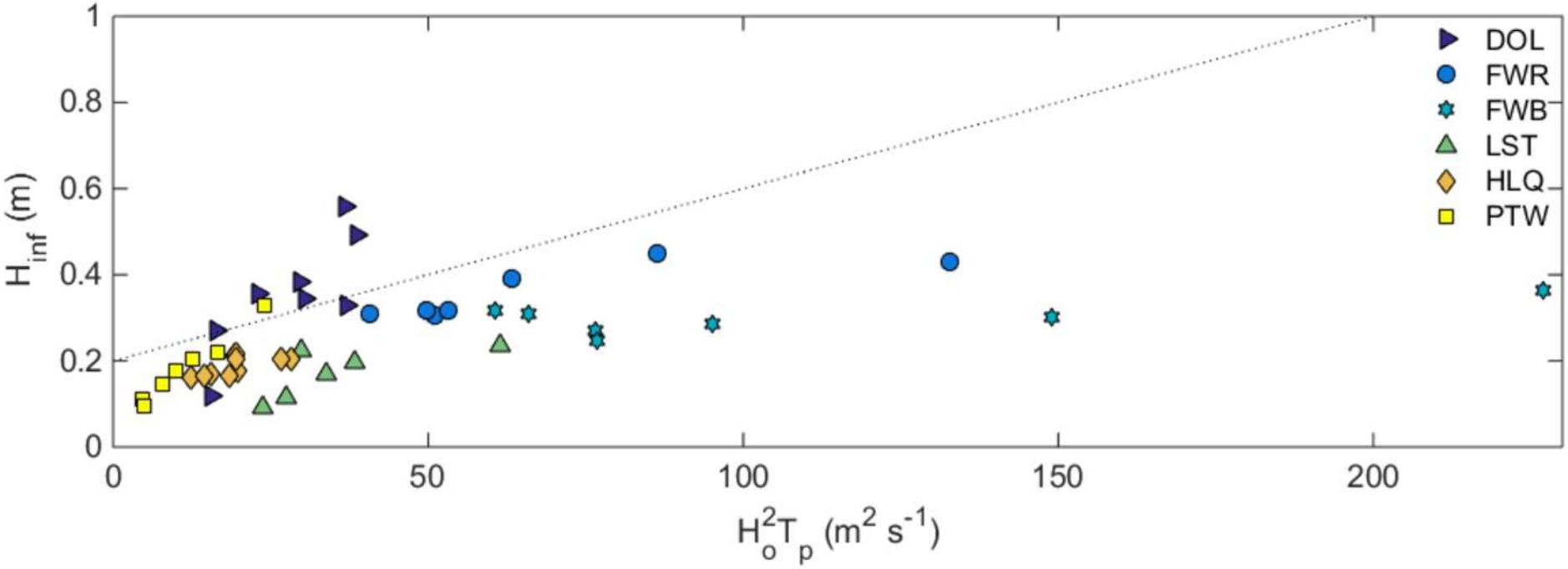
1
0.8
0.6
0.4
0.2
0
H_{inf} (m)
0
50
100
150
200
$H_o^2 T_p$ (m^2 s^{-1})
DOL
FWR
FWB
LST
HLQ
PTW

Figure 13.

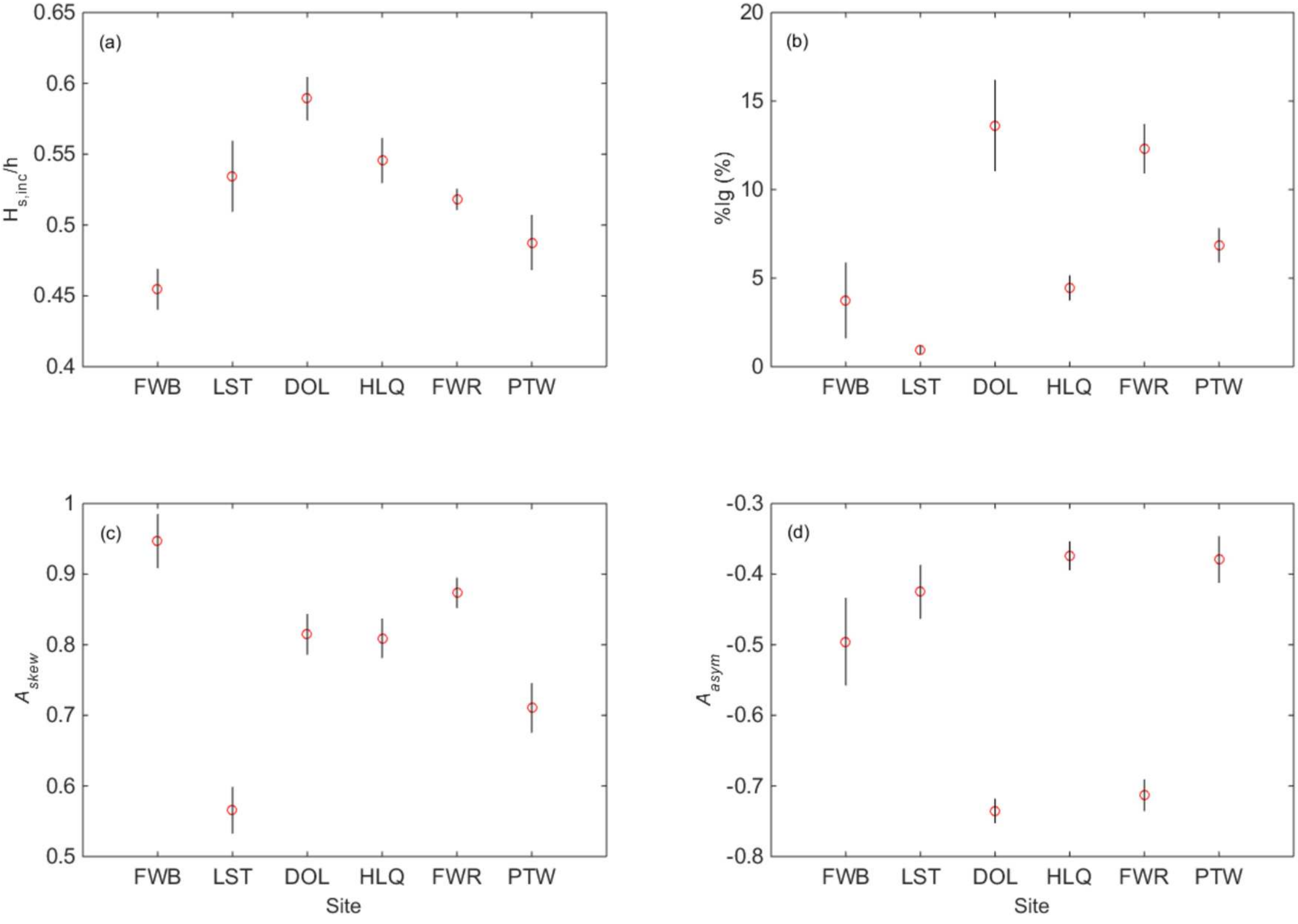
(a)
$H_{s,inc}/h$
0.65
0.6
0.55
0.5
0.45
0.4
FWB
LST
DOL
HLQ
FWR
PTW
(b)
%lg (%)
20
15
10
5
0
FWB
LST
DOL
HLQ
FWR
PTW
(c)
A_{skew}
1
0.9
0.8
0.7
0.6
0.5
FWB
LST
DOL
HLQ
FWR
PTW
Site
(d)
A_{asym}
-0.3
-0.4
-0.5
-0.6
-0.7
-0.8
FWB
LST
DOL
HLQ
FWR
PTW
Site

Figure 14.

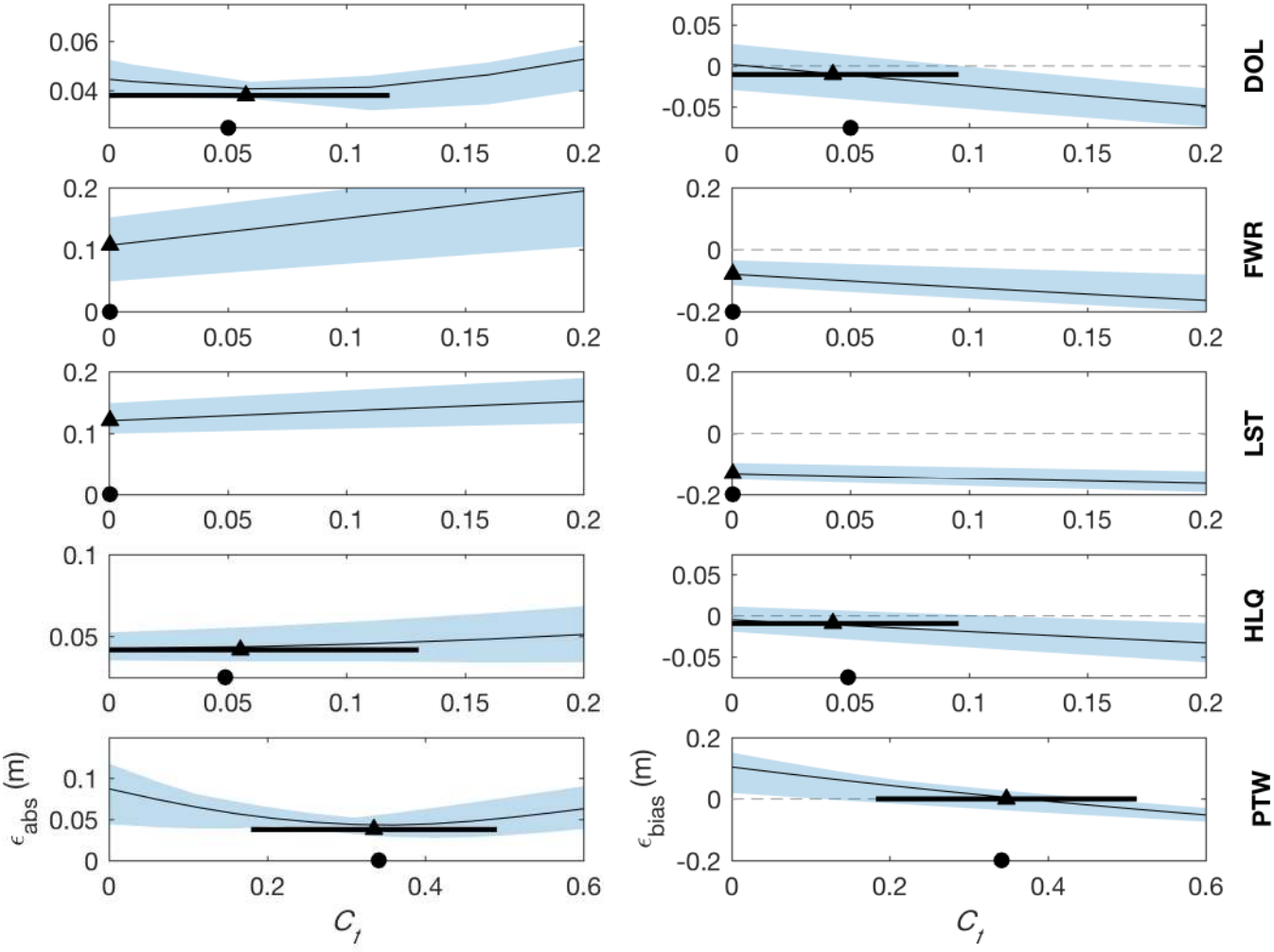
DOL
FWR
LST
HLQ
PTW
ϵ_{abs} (m)
ϵ_{bias} (m)
C_f
C_f

Figure 15.

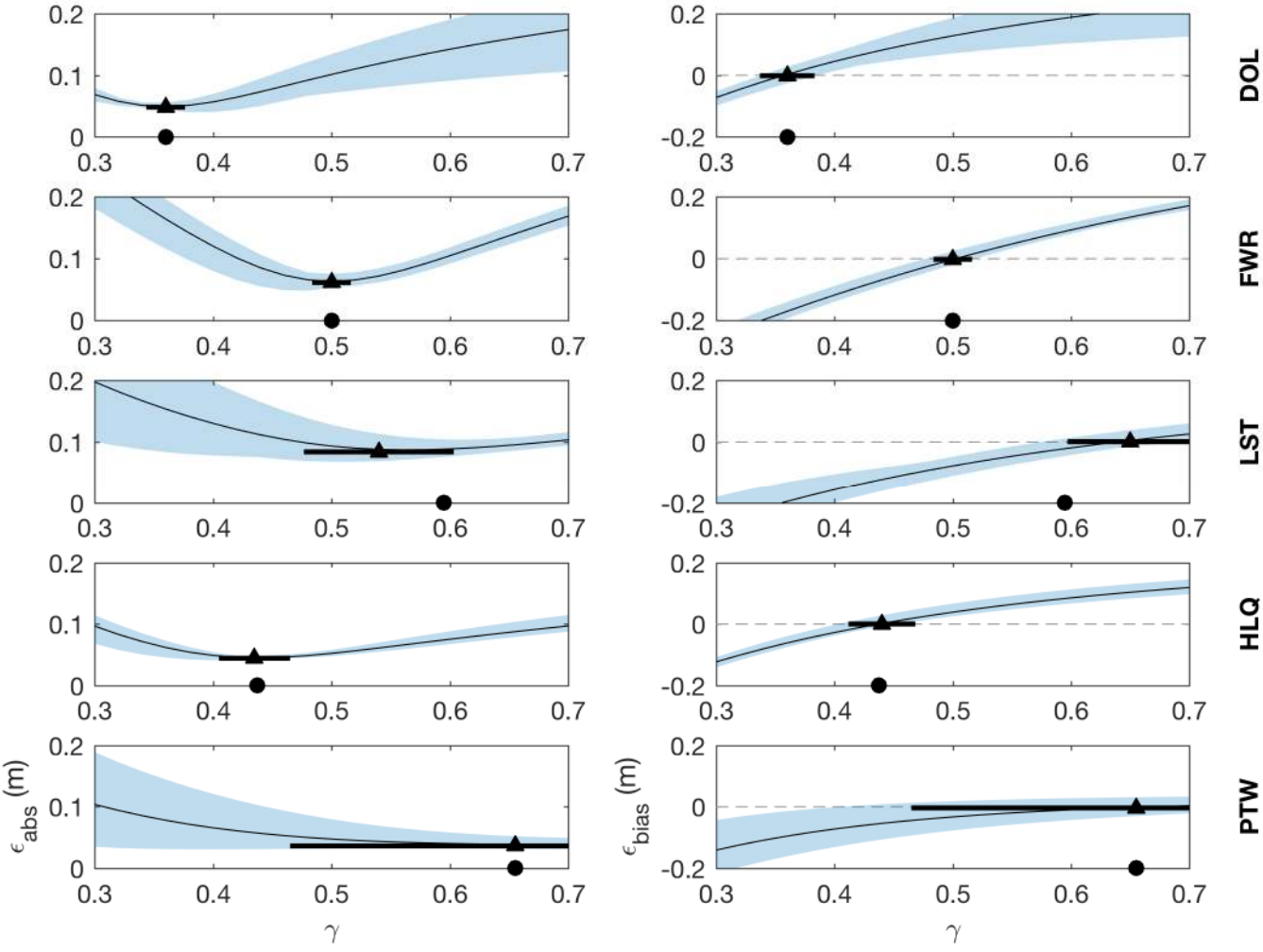
DOL
FWR
LST
HLQ
PTW
ϵ_{abs} (m)
ϵ_{bias} (m)
γ
γ

Figure 16.

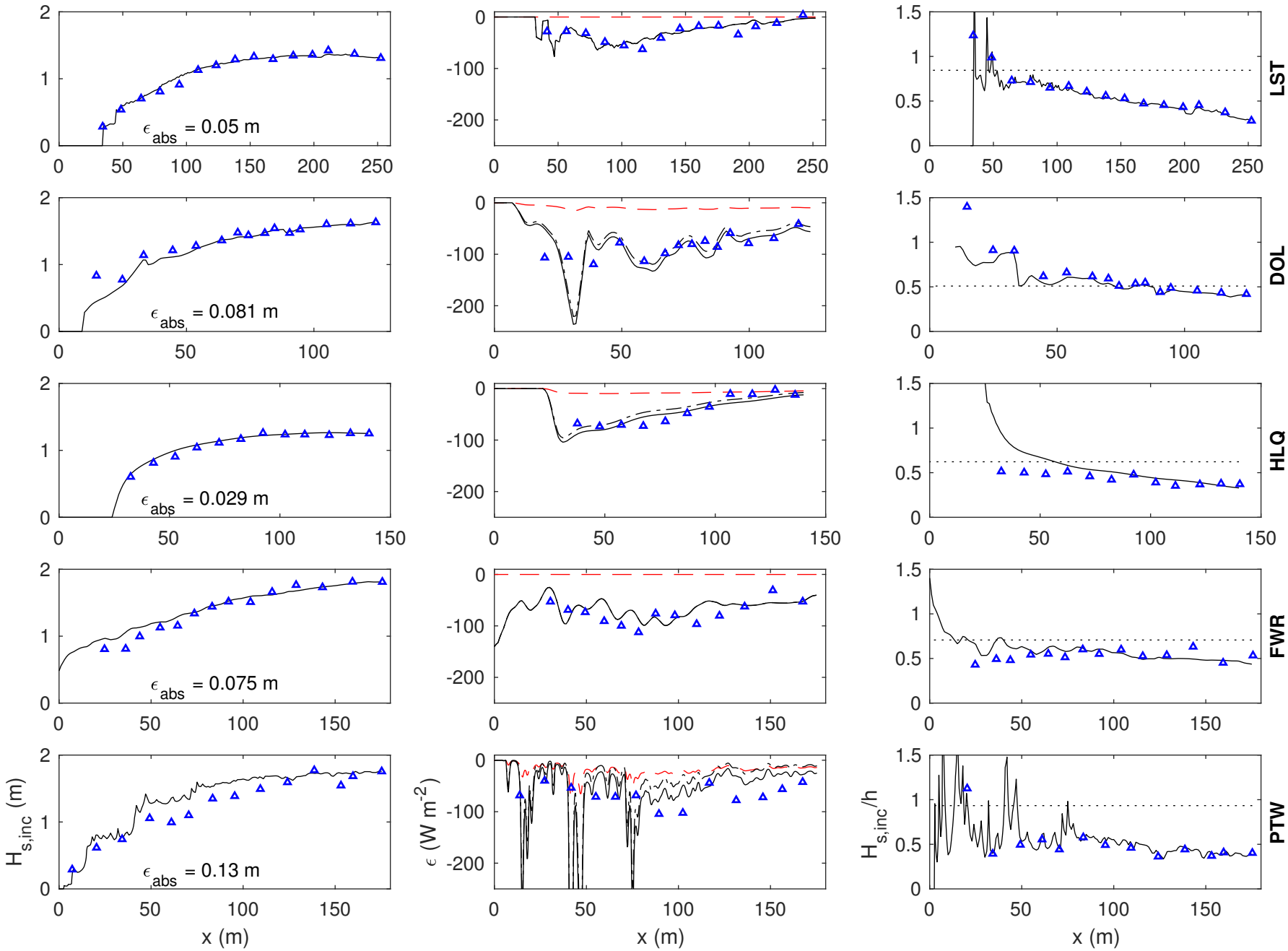
ϵ_{abs} = 0.05 m
ϵ_{abs} = 0.081 m
ϵ_{abs} = 0.029 m
ϵ_{abs} = 0.075 m
ϵ_{abs} = 0.13 m
$H_{s,inc}$ (m)
ϵ (W m^{-2})
$H_{s,inc}/h$
x (m)
x (m)
x (m)
LST
DOL
HLQ
FWR
PTW

Figure 17.

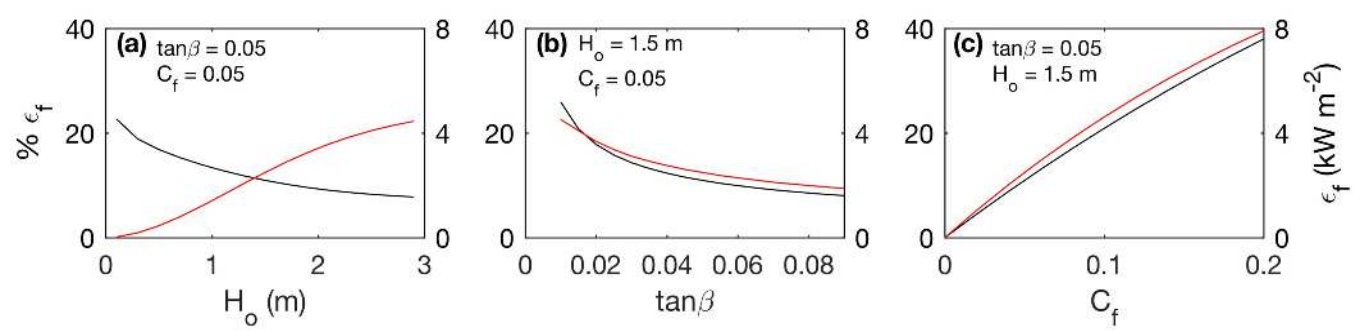
(a) tanβ = 0.05
C_f = 0.05
% ε_f
H_o (m)
(b) H_o = 1.5 m
C_f = 0.05
tanβ
(c) tanβ = 0.05
H_o = 1.5 m
C_f
ε_f (kW m^-2)